

RESEARCH ARTICLE | JULY 01 2024

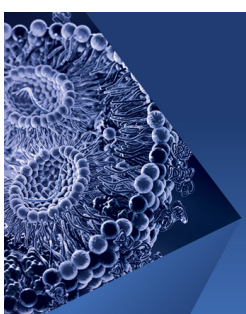
Unsteady wake and heat transfer characteristics of three tandem circular cylinders in forced and mixed convection flows

Hongjun Zhu (朱红钧)   ; Jiawen Zhong (钟家文)  ; Bin Liu (刘斌)  ; Tongming Zhou (周同明) 

 Check for updates

Physics of Fluids 36, 073602 (2024)

<https://doi.org/10.1063/5.0213990>



Physics of Fluids

Special Topic:

Flow and Lipid Nanoparticles

Guest Editors: Richard Braatz and Mona Kanso

[Submit Today!](#)

 AIP
Publishing

Unsteady wake and heat transfer characteristics of three tandem circular cylinders in forced and mixed convection flows

Cite as: Phys. Fluids **36**, 073602 (2024); doi: [10.1063/5.0213990](https://doi.org/10.1063/5.0213990)

Submitted: 15 April 2024 · Accepted: 9 June 2024 ·

Published Online: 1 July 2024



[View Online](#)



[Export Citation](#)



[CrossMark](#)

Hongjun Zhu (朱红钧)^{1,a)} Jiawen Zhong (钟家文)¹ Bin Liu (刘斌)^{2,3} and Tongming Zhou (周同明)⁴

AFFILIATIONS

¹State Key Laboratory of Oil and Gas Reservoir Geology and Exploitation, Southwest Petroleum University, Chengdu 610500, China

²Faulty of Science, Agriculture and Engineering, Newcastle University, Newcastle Upon Tyne NE1 7RU, United Kingdom

³Newcastle Research and Innovation Institute, Newcastle University in Singapore, Singapore 609607, Singapore

⁴Department of Civil, Environmental and Mining Engineering, The University of Western Australia, Crawley, Washington 6009, Australia

^{a)}Author to whom correspondence should be addressed: zhuhj@swpu.edu.cn

ABSTRACT

In natural convection (high Richardson number Ri), a high Prandtl number (Pr) leads to thinner thermal boundary layers, enlarging the thermal gradient and hence the enhancement of buoyancy effect. In forced convection (low Ri), a high Pr introduces thicker velocity boundary layers. In mixed convection scenarios, where both forced and natural convection are significant, the interaction between Pr and Ri determines the resultant flow pattern and heat transfer characteristic. Three tandem circular cylinders with an identical spacing ratio of 4.0 in both forced and mixed convection flows were numerically investigated by using finite element method. The computations were carried out in the range of $Pr = 5\text{--}50$ and $Ri = 0\text{--}2$ at a low Reynolds number of $Re = 150$. The results of the squared strain rate and the vorticity shed light on the enstrophy transfer process. Thermal plume structures in the far wake originate from the upper dispersed vortices due to the high superimposed buoyancy at low Pr , while they are suppressed at high Pr . The increase in Pr plays a role as the flow stabilization, while the growth of Ri plays the reverse role. The time-averaged velocity, pressure coefficient, and temperature become more asymmetrical at high Ri . The Nusselt number of the upstream cylinder is approximately equal to the empirical result without the consideration of thermal buoyancy. Due to the thermal buoyancy, the migration of shear layers along the cylinder surface leads to the frequency alteration and harmonic frequency in the drag, lift, and Nusselt coefficients.

Published under an exclusive license by AIP Publishing. <https://doi.org/10.1063/5.0213990>

I. INTRODUCTION

Convection heat transfer in the fluid–structure interaction has been widely attracting study, due to the underlying physics and extensive engineering applications such as chimney stacks, cooling rods, wire cables, and heat exchangers.^{1,2} The flow around a circular cylinder is mainly governed by the Reynolds number ($Re = \rho u_{in} D / \mu$, where ρ is the density of the fluid, u_{in} is the freestream velocity, and μ is the dynamic viscosity of fluid, D is the cylinder diameter), Prandtl number ($Pr = \nu/\kappa$, where ν is the kinematic viscosity of the fluid and κ is the thermal diffusivity), and Richardson number [$Ri = Gr/Re^2$, where Gr is the Grashof number, $Gr = g\beta(T_w - T_\infty)D^3/\nu^2$, g is the gravitational acceleration, β is the volume expansion coefficient, T is the temperature with the subscripts “ w ” and “ ∞ ” representing the wall and free-stream, respectively]. It is known that forced convection occurs at

$Ri < 0.1$, where the influence of thermal buoyancy is negligible. Natural convection emerges at $Ri > 10$, and the heat between the flow and structure is conducted through heat convection. For mixed convection, i.e., $0.1 < Ri < 10$, the thermal buoyancy should be considered, and the angle between the inlet velocity and buoyancy direction α is an important parameter.³ Three typical α cases are the horizontal cross-flow ($\alpha = 90^\circ$), the parallel flow ($\alpha = 0^\circ$), and the counter-flow ($\alpha = 180^\circ$). It was found that the flow pattern behind the circular cylinder becomes asymmetrical in the horizontal cross-flow,⁴ and the wake structure is accordingly complicated.

Flow past a heated circular cylinder is a documented bench mark issue, as reported in a vast amount of literature. Badr⁵ numerically simulated a horizontal circular cylinder in the mixed convection at $1 < Re < 40$, $0 < Ri < 5$ and $Pr = 0.7$. The distribution of vorticity,

pressure, and local Nusselt number around the cylinder surface was obviously different from the forced convection case. The experiments conducted by Kieft *et al.*⁶ found that the wake behind a heated cylinder deflected to the gravity direction at $0 < Ri < 1$, presenting an unexpected direction, which is the opposite direction of buoyancy. Later, detailed experiments and numerical simulations illustrate that this effect is generated due to the strength difference between two-row vortices.⁷ An analysis of the vorticity sources present during the formation process shows that the thermally induced baroclinic vorticity production is the main reason. Maas *et al.*⁸ pointed out that the warm fluid is initially collected in the coherent vortex structures shed from the cylinder for $Ri < 1$, and these structures introduce the thermal plumes far away from the cylinder. In contrast, the upward buoyancy force prevents the formation of coherent vortex structures and hence the plumes are already formed just behind the cylinder when $Ri > 1$. Comprehensive reviews^{9–11} on the investigation of a circular cylinder in forced convection flow indicate the emergence of vortex shedding at $Re = 47$. Biswas and Sarkar¹² confirm that the characteristics of the flow structure of a circular cylinder can be altered by the cross-thermal buoyancy. They¹² found that the vortex shedding starts at $Re = 10$ when $Ri = 1.4$ and shifts to $Re = 45$ when $Ri = 1.985$. Sarkar *et al.*¹³ investigated the effects of Pr and Ri on the wake dynamics and heat transfer past a circular cylinder in both forced and mixed convective flows for $80 \leq Re \leq 180$, $0.7 \leq Pr \leq 100$, and $0 \leq Ri \leq 2$. Under the action of cross thermal buoyancy, the Strouhal number of vortex shedding decreases with increasing the Pr . The upward drift of vortex structures and streamlines decreases accordingly. Thus, increasing the Pr could stabilize the flow.¹³ The near-wake region regains symmetry about the centerline when Pr is as large as 100.¹⁴ Zhu *et al.*¹⁵ pointed out that stronger nonlinear features exist in the wake of mixed convection subject to cross buoyancy as Ri increases, compared with the forced convection. The effect of cross-thermal buoyancy on the vortex-induced vibration (VIV) of a circular cylinder was numerically investigated by Grag *et al.*¹⁶ and Liu and Zhu.¹⁷ Grag *et al.*¹⁶ observed the VIV suppression at $Re = 50$ and $1 \leq Ri \leq 2$, and the galloping at $3 \leq Ri \leq 4$ for $50 \leq Re \leq 150$. Liu and Zhu¹⁷ found the secondary VIV lock-in in the cases of $Ri = 2$ and $Pr \leq 2$ when the reduced velocity is larger than 7.

Multiple cylinders are usually arranged in various configurations, i.e., tandem, side-by-side, and staggered. Among them, flow around tandem cylinders experiences the most complex behavior. The downstream cylinder experiences a complicated wake interference because of the interaction with the shear layers or/and vortices generated from the upstream cylinder. Houssem and Mohamed¹⁸ numerically investigated two isothermal tandem circular cylinders in mixed convection flow. Due to the existence of thermal buoyancy, the drag coefficient is augmented and the average Nusselt number of the downstream cylinder is larger than the upstream one. Houssem *et al.*¹⁹ found the increase in the Richardson number results in the amplification of drag coefficient, whereas the reduction of heat transfer rate of the upstream cylinder. The wall effect becomes stronger at higher block ratio.^{18,19} Zafar and Alam³ numerically investigated a heated circular cylinder submerged in the wake of another un-heated cylinder at $Re = 100$, $0 \leq Ri \leq 2$ with a spacing ratio of $1.2 \leq L/D \leq 5$. The result indicates that as Ri increases, downwash and upwash flows are generated before and after the heated cylinder, enhancing the heat transfer. Furthermore, Chaitanya *et al.*¹ reported that the drag acting on the

cylinders decreases with the Re and Ri . By contrary, it increases with the increase in spacing ratio between two tandem heated cylinders.

The thermo-fluidic transport and interference between multiple cylinders are far from well understood. Meanwhile, the dependence of the hydrodynamic coefficient for each cylinder on Ri and Pr needs to be figured out. Therefore, the aim of the present work is to explore the effect of thermal cross-buoyancy on the wake flow and heat transfer characteristics around three tandem heated circular cylinders. The thermal buoyancy is introduced by varying Ri and Pr . The remainder of this paper is organized as follows. The governing equations and the derived numerical formulations are first introduced in Sec. II. Section III illustrates the computational domain and the boundary conditions. After that, the mesh independence and the validation of derived numerical formulations are presented in Sec. IV. The numerical results are discussed in Sec. V. Finally, the conclusion is summarized in Sec. VI.

II. GOVERNING EQUATIONS AND NUMERICAL FORMULATION

The unsteady Navier–Stokes equations are coupled with the conservation of energy equation in this work to simulate the heat transfer and flow around three tandem cylinders. The governing equations and associated boundary and initial conditions are expressed as

$$\nabla \cdot \mathbf{u} = 0, \quad \forall \mathbf{x} \in \Omega^f(t), \quad (1a)$$

$$\rho(\partial_t \mathbf{u} + (\mathbf{u} \cdot \nabla) \mathbf{u}) = \nabla \cdot \boldsymbol{\sigma} + \rho \mathbf{g}, \quad \forall \mathbf{x} \in \Omega^f(t), \quad (1b)$$

$$\partial_t T + (\mathbf{u} \cdot \nabla) T = \alpha \nabla^2 T, \quad \forall \mathbf{x} \in \Omega^f(t), \quad (1c)$$

$$\mathbf{u} = \tilde{\mathbf{u}}; \quad T = \tilde{T}, \quad \forall \mathbf{x} \in \Gamma_D^f(t), \quad (1d)$$

$$\boldsymbol{\sigma} \cdot \mathbf{n} = \tilde{h}; \quad \boldsymbol{\alpha}(\nabla T) \cdot \mathbf{n} = \tilde{q}, \quad \forall \mathbf{x} \in \Gamma_N^f(t), \quad (1e)$$

$$\mathbf{u} = \tilde{\mathbf{u}}_0; \quad T = \tilde{T}_0, \quad \forall \mathbf{x} \in \Omega^f(0), \quad (1f)$$

where \mathbf{u} is the flow velocity vector, \mathbf{x} is the position vector, ρ is the fluid density, $\mathbf{g} = [0, -g]' = [0, -9.81]'$ is the gravitational acceleration vector, t is the flow time, $\boldsymbol{\sigma}$ is the Cauchy stress tensor, T is the temperature, α is the thermal diffusivity, $\tilde{\mathbf{u}}$ represents the prescribed flow velocity imposed along the boundaries, \tilde{T} represents the prescribed temperature imposed along the boundaries, \mathbf{n} is the unit outward normal vector of the element's edge, \tilde{h} and \tilde{q} are the prescribed convection transfer coefficient and heat flux along the boundaries, respectively, $\tilde{\mathbf{u}}_0$ represents the initial flow velocity, \tilde{T}_0 represents the initial temperature, and Γ_D and Γ_N denote the Dirichlet and Neumann domain boundaries, respectively. The term $\partial_t(\cdot)$ represents the partial derivative with respect to the flow time. The Cauchy stress tensor ($\boldsymbol{\sigma}$) is a function of \mathbf{u} and p , defined as

$$\boldsymbol{\sigma} = -p\mathbf{I} + 2\mu\boldsymbol{\varepsilon}, \quad (2a)$$

$$\boldsymbol{\varepsilon} = \frac{1}{2} [\nabla \mathbf{u} + (\nabla \mathbf{u})'], \quad (2b)$$

where \mathbf{I} is the Kronecker matrix, μ is the dynamic viscosity, $\boldsymbol{\varepsilon}$ is the strain rate tensor, and the superscript ('') is a transpose operator. The fluid density is assumed to be uniform, except for regions with a significant influence of buoyancy. This assumption leads to Boussinesq approximation (BA), where the deviation of local fluid density is taken as a function of temperature difference. In mixed convection, the influence of buoyancy action on fluid inertia is non-negligible. Because of

the small density variation, a general incompressible flow approximation is adopted. Assuming the density is a function of temperature, $\rho = \rho(T)$, elementary thermodynamics states that $\beta = -(\partial \rho / \partial T) / \rho$. Hence, the density of fluid at a given pressure depends on the temperature, which can be written as

$$\rho = \rho_0 [1.0 - \beta(T - T_\infty)], \quad (3)$$

where ρ_0 is the reference fluid density. These considerations lead to the Boussinesq approximation in the y -component of conservation of momentum (along gravitational direction).

The simulation in this work was conducted with dimensionless variables. Introducing the dimensionless groups in Eq. (4), where $u_{in} = 1$, the governing equations in Eq. (1) can be rewritten in the dimensionless form, as seen in Eq. (5) as follows:

$$\begin{aligned} \mathbf{x}^* &= \frac{\mathbf{x}}{D}, \quad \mathbf{u}^* = \frac{\mathbf{u}}{u_{in}}, \quad \tau = \frac{tu_{in}}{D}, \\ p^* &= \frac{p + \rho_0 g z}{\rho_0 u_{in}^2}, \quad T^* = \frac{T + T_\infty}{T_w - T_\infty}, \end{aligned} \quad (4)$$

where the superscript (*) indicates the proposed dimensionless groups, τ and T^* are the dimensionless time and temperature, respectively. The value of z is the elevation height in the direction of gravitational acceleration

$$\nabla \cdot \mathbf{u}^* = 0, \quad \forall \mathbf{x}^* \in \Omega^f(\tau), \quad (5a)$$

$$\begin{aligned} \partial_\tau \mathbf{u}^* + (\mathbf{u}^* \cdot \nabla) \mathbf{u}^* &= -\nabla p^* + \frac{1}{Re} \nabla \cdot (\nabla \mathbf{u}^* + (\nabla \mathbf{u}^*)'), \\ &\quad - \left(\frac{Gr}{Re^2} \mathbf{n}_g \right) T^*, \quad \forall \mathbf{x}^* \in \Omega^f(\tau), \end{aligned} \quad (5b)$$

$$\partial_\tau T^* + (\mathbf{u}^* \cdot \nabla) T^* = \frac{1}{RePr} \nabla^2 T^*, \quad \forall \mathbf{x}^* \in \Omega^f(\tau), \quad (5c)$$

$$\mathbf{u}^* = \tilde{\mathbf{u}}^*; \quad T^* = \tilde{T}^*, \quad \forall \mathbf{x}^* \in \Gamma_D^f(\tau), \quad (5d)$$

$$\left(-p^* \mathbf{I} + \frac{2}{Re} \varepsilon(\mathbf{u}^*) \right) \cdot \mathbf{n} = \tilde{\mathbf{h}}^*; \quad \left(\frac{1}{RePr} \nabla T^* \right) \cdot \mathbf{n} = \tilde{q}^*, \quad \forall \mathbf{x}^* \in \Gamma_N^f(\tau), \quad (5e)$$

$$\mathbf{u}^* = \tilde{\mathbf{u}}_0^*; \quad T^* = \tilde{T}_0^*. \quad \forall \mathbf{x}^* \in \Omega^f(0), \quad (5f)$$

where $\mathbf{n}_g = [0, -1]$ is the unit vector of gravitational force.

The variables in Eq. (5) are spatially Discretized using a stabilized finite element formulation. A semi-discrete ordinary differential equation (ODE) is used for the temporal discretization. Similar to the conservation of momentum, the conservation of energy in Eq. (5c) involves a nonlinear advection term $(\mathbf{u}^* \cdot \nabla) T^*$, causing spurious oscillations in fluid velocity. Hence, the residual-based stabilized finite element formulations, i.e., Galerkin least squares (GLS)²⁰ and pressure stabilizing Petrov Galerkin (PSPG),²¹ are employed to stabilize the spurious oscillations in fluid velocity by introducing the numerical diffusion and the circumventing of the Ladyzhenskaya–Babuska–Brezzi (LBB) condition in the coupled velocity-pressure field.¹⁷

In this study, a number statistical quantities are defined to quantify the complexity of dynamics in mixed convection. For instance, the time-averaged hydrodynamic coefficients ($C_{D,\text{mean}}$ and $C_{L,\text{mean}}$) and the standard deviation hydrodynamic coefficients ($C_{D,\text{rm}}$ and $C_{L,\text{rms}}$) are defined as

$$C_{D,\text{mean}} = \frac{1}{N} \sum_{i=1}^N C_{D,i}, \quad (6)$$

$$C_{L,\text{mean}} = \frac{1}{N} \sum_{i=1}^N C_{L,i}, \quad (7)$$

$$C_{D,\text{rms}} = \sqrt{\frac{1}{N} \sum_{i=1}^N (C_{D,i} - C_{D,\text{mean}})^2}, \quad (8)$$

$$C_{L,\text{rms}} = \sqrt{\frac{1}{N} \sum_{i=1}^N (C_{L,i} - C_{L,\text{mean}})^2}, \quad (9)$$

where N is the number of sample data in the time series. The $C_{D,i}$ and $C_{L,i}$ are the dimensionless traction forces exerted on the cylinder in the x and y directions, respectively.

In the simulation, the normalized temperature on the surface of three tandem cylinders is identically defined as 1 ($T^* = 1$). The local Nusselt number $Nu_{(\theta)}$ of a specific location on the cylinder surface and the Nu of the entire cylinder surface are defined as

$$Nu_{(\theta)} = -\nabla T^*_{(\theta)} \cdot \mathbf{n}_{(\theta)}, \quad (10)$$

$$Nu = \frac{1}{\ell} \int_{\theta=0}^{\ell} Nu_{(\theta)} d\theta. \quad (11)$$

The unconditionally stable second-order accurately generalized- α time integration scheme is employed for both fluid and structure solvers to march the solutions in time, which has been proven to be feasible by Chung and Hulbert²² and Jansen *et al.*²³

III. DESCRIPTION OF PHYSICAL PROBLEM

In this two-dimensional (2D) forced and mixed convection flow and heat transfer problem, the employed computational domain and associated boundaries are shown in Fig. 1. The upstream circular cylinder (denoted as C1) is placed at the coordinate origin ($x = 0, y = 0$), and the computational domain extends $50D$ downstream and $10D$ in front of C1 center. The streamwise spacing ratio between the upstream cylinder and the middle cylinder (denoted as C2) is identical to that between the middle and downstream cylinders (denoted as C3), kept at $L/D = 4$. Three tandem circular cylinders are placed centrally in the transverse direction, $25D$ from both the upper and lower boundaries. Hence, the blocking ratio is 2%, meeting the requirement of blocking ratio less than 6%.^{24,25}

A similar setting has been examined in previous work.²⁶ The main difference is the consideration of the cross thermal buoyancy effect in this work. The boundary conditions which are used to solve the governing equations are as follows:

- Inlet: Dirichlet-type boundary condition, $u^* = 1, v^* = 0$, and $T^* = 0$;
- Outlet: Neumann-type boundary condition, $h^* = 0$ and $q^* = 0$;
- Upper and lower boundaries: symmetry boundary condition, $v^* = 0, h^* = 0$, and $q^* = 0$;
- Cylinders' surface: no-slip boundary condition, $u^* = 0, v^* = 0$, and $T^* = 1$.

Previous literature has extensively reported the numerical results of flow around a circular cylinder in the ranges of $Re = 1\text{--}180$, $Pr = 0.7\text{--}100$, and $Ri = 0\text{--}2$. Nevertheless, most of them focus on the

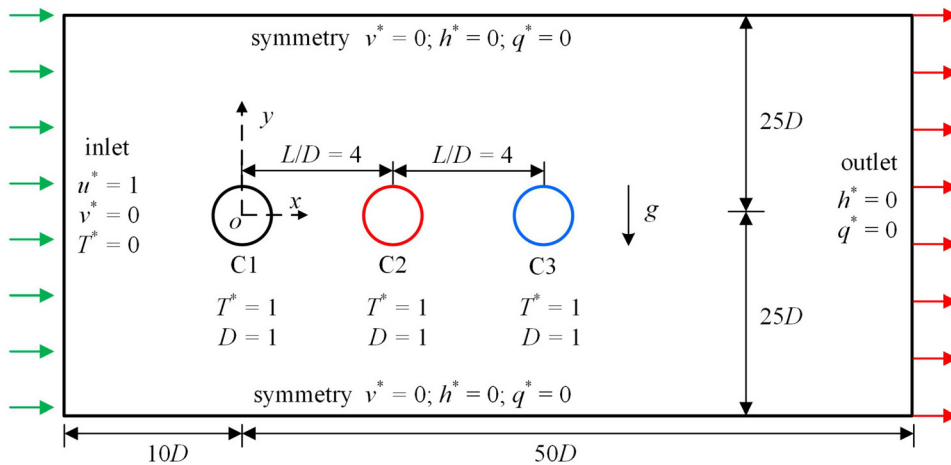


FIG. 1. Computational domain and boundary conditions.

effect of a single parameter. The research considering the effects of both Pr and Ri is scanty. Although Sarkar *et al.*¹³ have examined the combined effect of Pr and Ri in the ranges of $0.7 \leq Pr \leq 100$ and $0 \leq Ri \leq 2$, their study was limited to a single cylinder. To fill the research gap, therefore, the hydrodynamics and heat transfer of three tandem cylinders in the ranges of $5 \leq Pr \leq 50$ and $0 \leq Ri \leq 2$ are numerically examined in this work at a fixed Reynolds number of $Re = 150$.

IV. MESH INDEPENDENCE AND CODE VALIDATION

A. Mesh independence

The computational domain is divided into triangular grids using Gmsh, as shown in Fig. 2(a). The boundary-layer mesh consists of structural grids along the cylinders' surface. Each cylinder perimeter is Discretized with 120 elements, as depicted in Fig. 2(b). The height of the first boundary-layer mesh close to the cylinder surface is below the linear viscous sublayer $y^+ = 0.5$, where y^+ is the dimensionless wall distance. The mesh is refined in each rectangular region encompassing the target cylinder, and the growth rate in the rectangular region is less than 1.03.

The mesh convergence test was performed first for the flow over three circular cylinders at $Ri = 2$ and $Pr = 5$, where the Courant-Friedrichs-Lowy (CFL) value was kept at 0.5. As shown in Table I, $C_{L,\text{rms}}$ and Nu_{mean} represent the lift coefficient and the Nusselt number, respectively. The maximum difference is found in $C_{L3,\text{rms}}$ when comparing the results of M1 and M2. Nevertheless, the maximum difference is less than 5%. Therefore, the mesh resolution of M2 is utilized for the simulations in this study.

B. Code validation

The derived numerical formulation was validated for the flow around a heated isolated circular cylinder at $Pr = 1$ and 10 .¹⁵ The mean Nusselt numbers agree well with the literature. Furthermore, the case of three tandem circular cylinders in forced convection ($Ri = 0$) at $L/D = 5$ and $Re = 160$ is also validated, as shown in Table II. The hydrodynamics coefficients ($C_{D,\text{mean}}$ and $C_{L,\text{rms}}$) and Strouhal number (St) are calculated and compared with reported data in the previous

literature.^{27,28} The maximum error found in $C_{L,\text{rms}}$ is within 10% for the downstream cylinder, suggesting a reasonable accuracy.

V. RESULTS AND DISCUSSION

A. The dynamics of enstrophy transfer in hydrodynamics

In the present investigation, the vortex shedding process under the influence of buoyancy at low Reynolds numbers was analyzed by calculating the contours of both ω and γ . Specifically for $Pr = 7$ and 50 and for the Richardson number at $Ri = 0$ and 2.0, the spatial gradients of ω and γ varying over time were calculated to identify the effect of buoyancy on vortex shedding. The adequate parameter used to describe the vorticity accumulation and structure formation is the squared strain rate minus the square of the vorticity.^{7,29,30}

$$\gamma = \frac{1}{2}(\sigma_1^2 + \sigma_2^2 - \omega^2), \quad (12a)$$

$$\sigma_1 = \frac{\partial u}{\partial x} - \frac{\partial v}{\partial y}, \quad (12b)$$

$$\sigma_2 = \frac{\partial v}{\partial x} + \frac{\partial u}{\partial y}, \quad (12c)$$

$$\omega = \frac{\partial v}{\partial x} - \frac{\partial u}{\partial y}, \quad (12d)$$

where σ_2 is the shear rate and ω is the vorticity. The growth of these gradients of ω and γ is related to the transfer of enstrophy (vorticity) to the small scale motion of the fluid. The gradients of vorticity tend to grow exponentially in a region where the squared magnitude of the rate of strain exceeds the squared magnitude of the rate of rotation.³⁰ If the γ becomes negative, the motion is elliptical. However, a positive γ corresponds to hyperbolic motion.¹² In fact, Weiss³⁰ showed that $\gamma < 0$ indicates the elliptic region signifying the accumulation of vorticity with increasing the local circulation, whereas $\gamma > 0$ indicates the hyperbolic region signifying the stretching of vorticity that prevents the growth of coherent structure. Therefore, in the elliptic region, coherent vortex structures emerge, while in the hyperbolic region, the strain rate becomes the dominant one, resulting in the stretching and deformation of fluid elements.

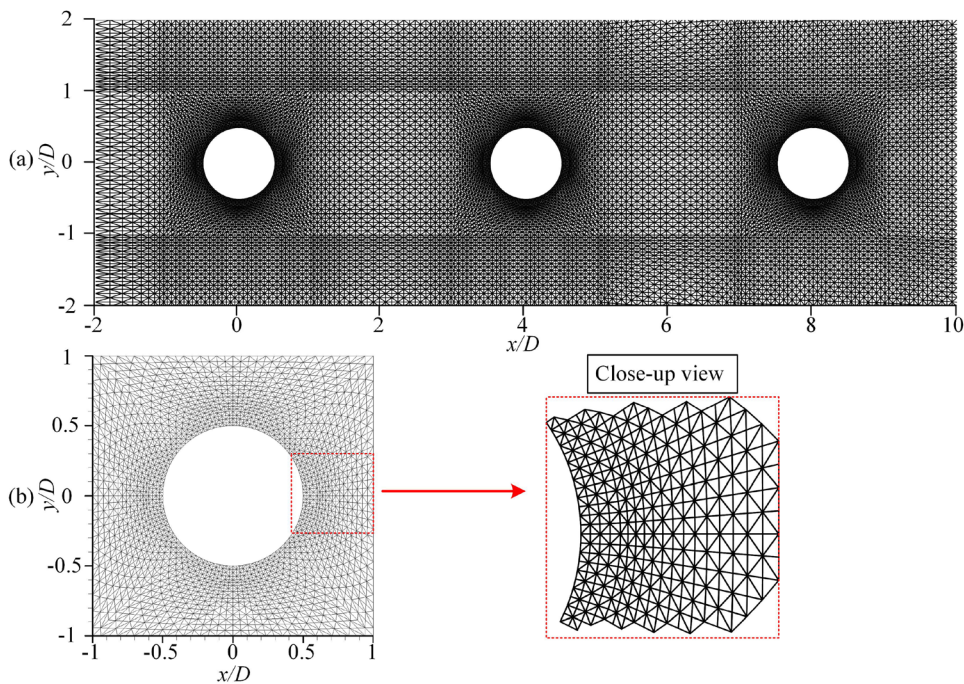


FIG. 2. Finite-element mesh: (a) grid distribution around three cylinders and (b) the grids in the vicinity of one cylinder and the close-up view of the boundary-layer elements.

TABLE I. Results for mesh dependency validation.

Mesh	Elements	$C_{L1,\text{rms}}$	$Nu_{1,\text{mean}}$	$C_{L2,\text{rms}}$	$Nu_{2,\text{mean}}$	$C_{L3,\text{rms}}$	$Nu_{3,\text{mean}}$
M1	180 528	0.479 (reference)	13.794 (reference)	1.227 (reference)	12.470 (reference)	0.362 (reference)	10.031 (reference)
M2	141 738	0.479 (0.00%)	13.449 (2.50%)	1.210 (1.39%)	12.235 (1.88%)	0.376 (3.87%)	10.266 (2.34%)
M3	102 064	0.465 (2.92%)	12.653 (8.27%)	1.106 (9.86%)	12.041 (3.44%)	0.390 (7.73%)	10.647 (6.14%)

Figure 3 shows the wake behavior of three tandem cylinders wake within a C_L cycle of C1 at $Pr = 7$ and $Ri = 0$. At $Ri = 0$, the thermal buoyancy effect can be neglected, due to the coefficient of thermal expansion being zero. Consequently, the time history of C_L for three tandem cylinders is symmetry along the line of $y = 0$. The vortex structure formation process is described in Fig. 3 for $Pr = 7$ and $Ri = 0$ with the contours of γ as well as the spatial gradients of ω within a vortex shedding cycle of C1 at four typical instants. The positive of γ represents the hyperbolic motion, signifying the occurrence of the constriction of the vorticity strand occurs. The negative of γ represents the

elliptic motion, which means that the gathering of the vorticity strand. The tip of the vorticity strand behind the C1 at t_0 is located at an area where $\gamma < 0$, i.e., $x \approx 1.06$ and $y \approx 0.22$ for the upper vortex, $x \approx 2.12$ and $y \approx -0.21$ for the lower vortex and then $x \approx 3.61$ and $y \approx 0.87$ for the former upper vortex. The vortex strand is squeezed apart from the cylinder by the contralateral curled boundary layer, produced at the vicinity of the cylinder surface. This constriction of the vorticity strand occurs in an area of $\gamma > 0$, indicating a dominant strain rate. Consequently, the shedding vortex alternately reattaches on the C2 surface. This phenomenon is called alternate reattachment mode in

TABLE II. Time-mean drag coefficient ($C_{D,\text{mean}}$), root-mean-squared value of lift coefficient ($C_{L,\text{rms}}$), and Strouhal number (St) of three tandem circular cylinders at $L/D = 5$ and $Re = 160$.

	Cylinder1			Cylinder2			Cylinder2		
	$C_{D,\text{mean}}$	$C_{L,\text{rms}}$	St	$C_{D,\text{mean}}$	$C_{L,\text{rms}}$	St	$C_{D,\text{mean}}$	$C_{L,\text{rms}}$	St
Duong <i>et al.</i> ²⁷	1.290	0.392	0.175	0.420	0.931	0.175	0.158	0.271	0.175
Zhu <i>et al.</i> ²⁸	1.287	0.385	0.171	0.411	0.922	0.171	0.151	0.264	0.171
Present	1.258	0.402	0.171	0.417	0.989	0.171	0.145	0.289	0.171
Max error	2.48%	4.42%	2.34%	1.46%	7.27%	2.34%	8.23%	9.47%	2.34%

previous literature.³¹ The alternately attached vortices stimulate the vortex shedding at the vicinity of C2 surface. Then, the shear layer of C3 surface is restrained by double row vortices behind C2, which is named as quasi-co-shedding mode.^{28,32} Moreover, the hyperbolic region exists between two adjacent vortices, where $\gamma > 0$, as shown in Fig. 3.

With the increase in Ri , under the influence of superimposed thermal buoyancy, the flow becomes unsteady and periodic. The thermal buoyancy brings about the asymmetry of the wake and induces the unsteadiness. It is found that the time histories of C_L for three cylinders asymmetric about the $y=0$ for $Ri > 0$. This means that the cross thermal buoyancy influences the hydrodynamic force coefficients, as shown in Fig. 4. A C_L cycle of C1 is marked in Fig. 4, and four moments are selected to exhibit the dynamics of enstrophy transfer in the wake. It is seen that the size of the area of $\gamma < 0$ is larger for the lower vortex than the upper vortex, which means that the accumulation of vorticities for the formation of a lower vortex blob takes place in a larger area and is highly affected by the strain rate.¹² The shedding of the lower vortex is more concentrated, while the upper vortex is dispersed. This is because of the effect of the high superimposed buoyancy. Further downstream, thermal plumes are generated from these structures, as shown in Fig. 4, at t_2 and $x \approx 11.67$ and $y \approx 2.22$. The upward buoyancy force seems to prevent the formation of the coherent vortex structures and the plumes are already formed close behind the cylinder.⁸ Meanwhile, a plume structure includes a negative vortex (dash line) and a positive vortex (solid line), where the hyperbolic region ($\gamma > 0$) is constricted in the middle, as shown in Fig. 4.

As the Prandtl number increases, the wake becomes more stable and the hydrodynamic coefficient approaches symmetric about $y=0$. Figure 5 shows the time histories of C_L for three cylinders and instantaneous enstrophy contours of γ and spatial gradients of ω at $Pr = 50$ and $Ri = 2$. It is also found that the size of the area of $\gamma < 0$ is larger for the lower vortex than the upper vortex. Meanwhile, the plume structure is suppressed as the Pr increases.

This part discusses the dynamics of enstrophy transfer under variables Pr and Ri , since the combined action of Pr and Ri determines the flow stability. It is seen from Figs. 3 and 4 that at a given Pr , the increase in Ri results in the increase in the thermal expansion coefficient β . According to Boussinesq approximation theory, the complicated enstrophy structure is caused by the decrease in gravity term and the increase in transverse buoyancy. In contrast, it is seen from Figs. 4 and 5 that at a given Ri , increasing the Pr leads to the decrease in thermal diffusivity and hence the thickened thermal boundary layers. Accordingly, the thermal convection gradient grows, giving rise to a smaller effective range of thermal buoyancy. Consequently, the enstrophy structure becomes more stable.

B. Hydrodynamic response subject to cross buoyancy

The vortex dynamics in mixed convection is rich of physics, since the hydrodynamics and buoyancy effect are strongly coupled in the wake. Figures 6–9 show the variations of hydrodynamic coefficients of the heated cylinder with respect to Pr . The inlet flow effect on the

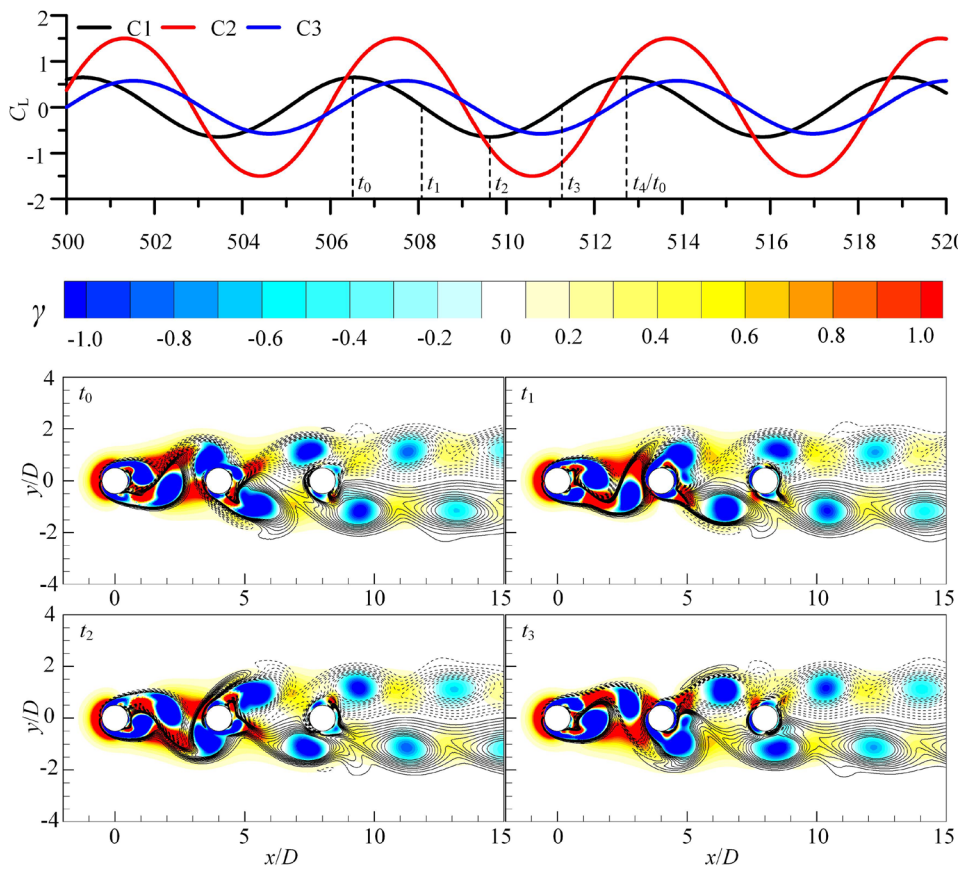


FIG. 3. Time histories of C_L for three cylinders and instantaneous enstrophy contours of γ and spatial gradients of ω at $Pr = 7$ and $Ri = 0$.

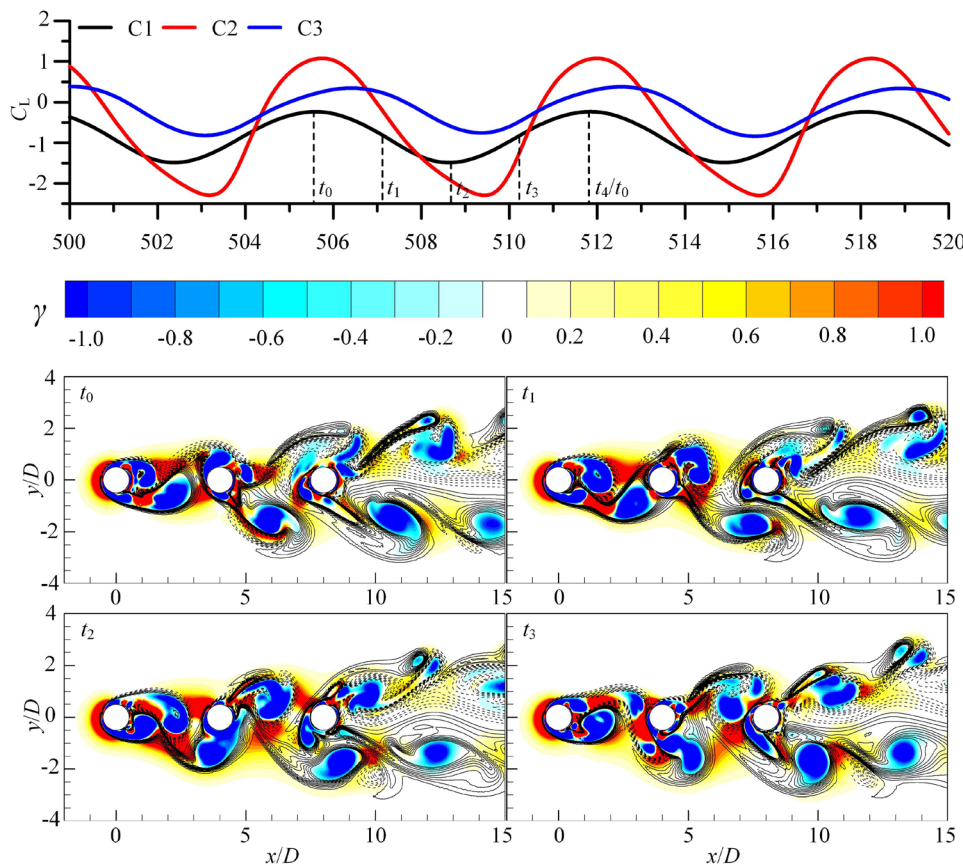


FIG. 4. Time histories of C_L for three cylinders and instantaneous enstrophy contours of γ and spatial gradients of ω at $Pr = 7$ and $Ri = 2$.

tandem cylinders at different Ri for very low Reynolds numbers is abundantly reported in the previous literature.^{1,18,19} However, the Prandtl number also strongly affects the force coefficients on the heated cylinder in mixed convection, which is widely discussed for a single cylinder.¹⁴ In Fig. 6, the variation of the time-averaged drag coefficients $C_{D,\text{mean}}$ [Eq. (6)] with Pr is plotted for various Ri . For the upstream cylinder C1 at $Ri = 0.5$, $C_{D,\text{mean}}$ increases with Pr and converges at $Ri = 0$. The value of $C_{D,\text{mean}}$ decreases with Ri at the same Pr and reaches a nearly constant value at $Ri > 0.5$. For the middle cylinder C2, the value of $C_{D,\text{mean}}$ decreases with Pr when $Ri > 0$ and reaches a nearly constant value at larger Pr . The asymptotic value of $C_{D,\text{mean}}$ of C2, however, depends on Ri . The stress distribution on the cylinder surface therefore does not converge to the case of $Ri = 0$. The downstream cylinder C3 is placed in the wake of C1 and C2, and the variation of $C_{D,\text{mean}}$ is very small. Under the influence of superimposed thermal buoyancy at $Ri > 0$, the $C_{D,\text{mean}}$ of C3 is larger than that in forced convection at $Ri = 0$.

Figure 7 shows the variation of the standard deviation drag coefficients $C_{D,\text{rms}}$ [Eq. (8)] with Pr . Generally, the value of each cylinder $C_{D,\text{rms}}$ decreases with Pr when $Ri > 0$ and reaches a nearly constant value at large Pr . The value of $C_{D,\text{rms}}$ increases with Ri at the same Pr , due to the influence of superimposed thermal buoyancy. Moreover, the deviation of the $C_{D,\text{rms}}$ of C1 is smaller than that of C2 and the deviation of $C_{D,\text{rms}}$ of C2 is smaller than that of C3, which means the fluctuation of the drag coefficient behind C1 increases.

In pure forced convection ($Ri = 0$), it can be observed that the time-averaged lift coefficient $C_{L,\text{mean}}$ [Eq. (7)] is zero in Fig. 8, which means the time history of lift coefficient is fluctuating. This is because the symmetry flow about the wake centerline.³³ However, the symmetry wake is destroyed and each cylinder encounters a negative $C_{L,\text{mean}}$ with the presence of cross thermal buoyancy when $Ri > 0$. The value of $C_{L,\text{mean}}$ increases (negative) with Pr and reaches a nearly constant value at larger Pr . However, the asymptotic values of $C_{L,\text{mean}}$ of C1 and C2 at larger Pr , depend on Ri , and the value of $C_{L,\text{mean}}$ of C3 converges to the case of $Ri = 0$.

Figure 9 shows the variation of the standard deviation lift coefficient $C_{L,\text{rms}}$ [Eq. (9)] with Pr . For the C1, the $C_{L,\text{rms}}$ of $Ri = 0.5$ decreases with Pr and converges to the case of $Ri = 0$, while the $C_{L,\text{rms}}$ at $Ri > 0.5$ decreases with Pr and reaches a nearly constant value at larger Pr . The asymptotic value of $C_{L,\text{rms}}$ of C1 at larger Pr , however, depends on Ri . The deviation of the $C_{L,\text{rms}}$ of C1 increases with the Ri at the same Pr . For the C2, under the effect of cross thermal buoyancy, the value the $C_{L,\text{rms}}$ when $Ri > 0$ is larger than $Ri = 0$. The $C_{L,\text{rms}}$ of C2 decreases with Pr , without the converge to the case of $Ri = 0$. For the C3, the fluctuation of the wake is enhanced with increasing the heat input (Ri), resulting in the increasing of $C_{L,\text{rms}}$. Moreover, as shown in Fig. 9, the $C_{L,\text{rms}}$ decreases with Pr and converges to the case of $Ri = 0$ at larger Pr .

The baroclinic around three heated cylinders reflects the production of vorticity within the flow domain, due to the temperature

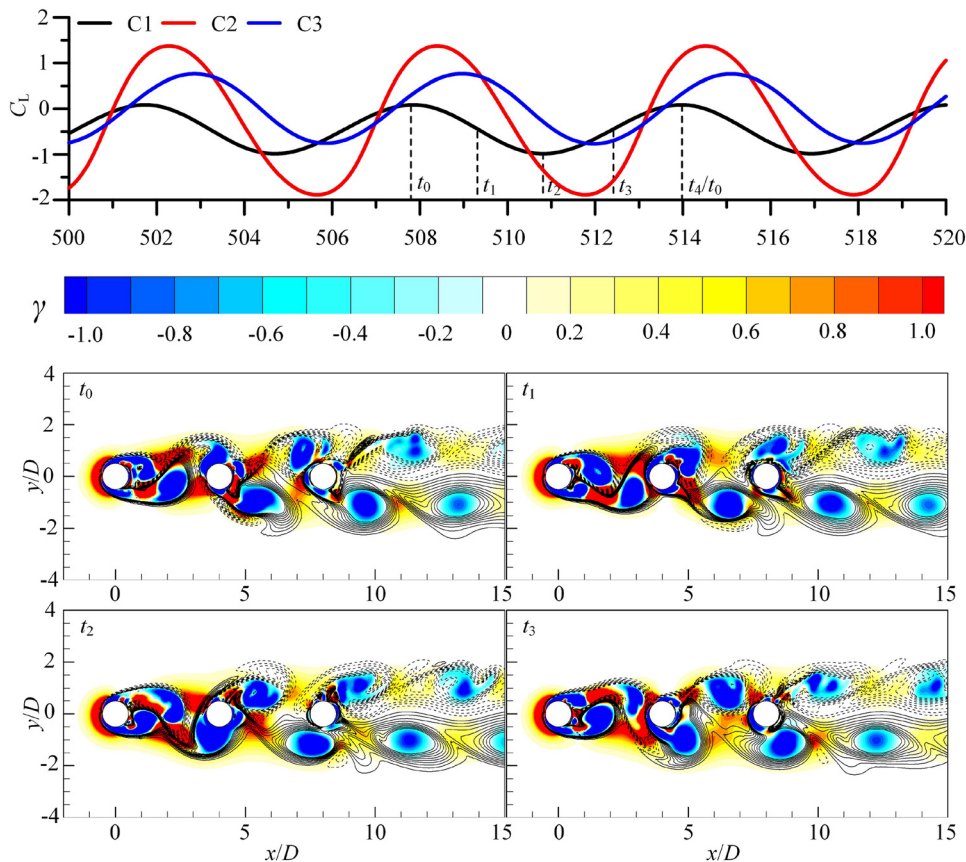


FIG. 5. Time histories of C_L for three cylinders and instantaneous enstrophy contours of γ and spatial gradients of ω at $Pr = 50$ and $Ri = 2$.

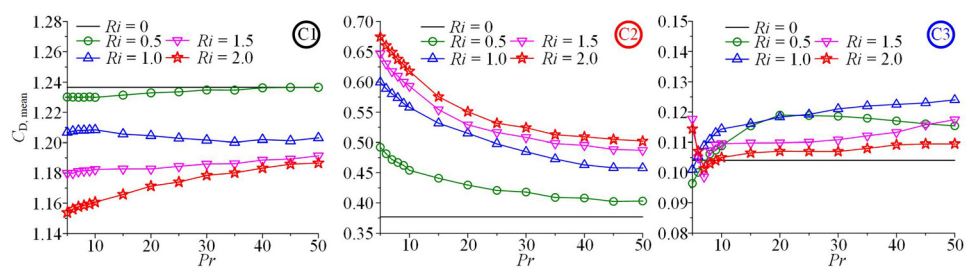


FIG. 6. Variation of the time-averaged drag coefficient $C_{D,\text{mean}}$ with respect to Pr : upstream cylinder C1 (left), middle cylinder C2 (middle), and downstream cylinder C3 (right).

gradient perpendicular to gravity. The pressure distribution is asymmetric about the centerline, explaining the characteristic of hydrodynamic coefficients. Under the influence of thermal buoyancy, the pressure drag of C1 is partially contributed from the transverse

component of baroclinic pressure, as it shifts from forced convection to mixed convection. As a result, the $C_{D,\text{mean}}$ of C1 is reduced. The redistributed portion contributes to an increase in the absolute value of $C_{L,\text{mean}}$. However, the $C_{D,\text{mean}}$ of C2 and C3 increases, due to the

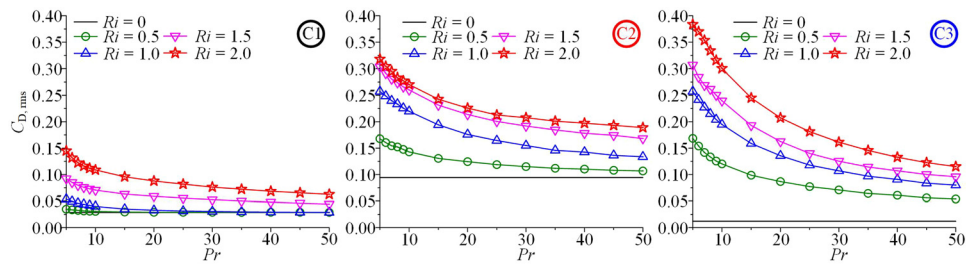


FIG. 7. Variation of the standard deviation drag coefficient $C_{D,\text{rms}}$ with respect to Pr : upstream cylinder C1 (left), middle cylinder C2 (middle), and downstream cylinder C3 (right).

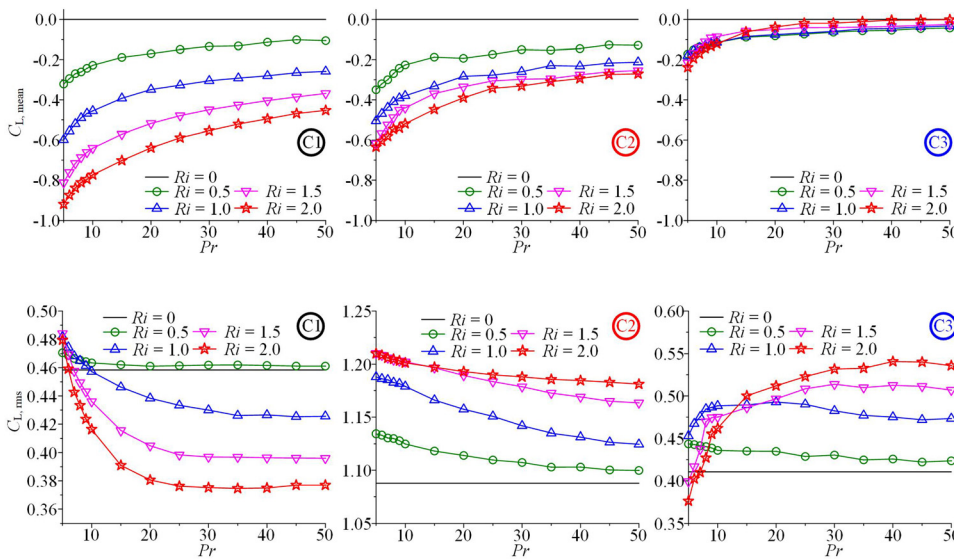


FIG. 8. Variation of the time average lift coefficient $C_{L,\text{mean}}$ with respect to Pr : upstream cylinder C1 (left), middle cylinder C2 (middle), and downstream cylinder C3 (right).

streamwise component of the baroclinic pressure. Similarly, the absolute value of $C_{L,\text{mean}}$ of them increases under the influence of the transverse component of baroclinic pressure in mixed convection.

C. Characteristics of heat convection

The mean Nusselt number Nu_{mean} is calculated by time averaging the local Nusselt number over the cylinder surface. Figure 10 shows the Nu_{mean} with Pr for various Ri . It can be seen that the value of Nu_{mean} increases with increasing Pr . This is due to the fact that increasing the Pr sets a higher temperature gradients over the cylinder surface and thereby a higher rate of heat transfer. For a single heated cylinder, Churchill and Bernstein³¹ proposed an empirical equation for the determination of Nu_{mean} , expressed as

$$Nu_{\text{mean}} = 0.3 + \frac{0.62Re^{1/2}Pr^{1/3}}{\left[1 + (0.4/Pr)^{2/3}\right]^{1/4}} \left[1 + \left(\frac{Re}{282000}\right)^{5/8}\right]^{4/5}. \quad (13)$$

Khan *et al.*³⁵ provided an empirical equation written as

$$Nu_{\text{mean}} = 0.593Re^{0.5}Pr^{0.333} \quad (14)$$

and Sarkar *et al.*¹³ proposed an empirical equation expressed as

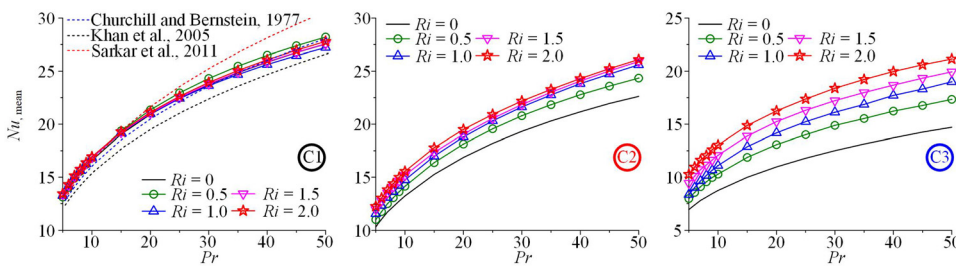


FIG. 9. Variation of the standard deviation lift coefficients $C_{L,\text{rms}}$ with respect to Pr : upstream cylinder C1 (left), middle cylinder C2 (middle), and downstream cylinder C3 (right).

$$Nu_{\text{mean}} = 0.459Re^{0.548}Pr^{0.373}. \quad (15)$$

The present work for the C1 approximates to the empirical formula³¹ in Eq. (13), as shown in Fig. 10. Since the C1 directly faces the incoming flow, the heat exchange mainly occurs on its surface, with the C2 and C3 decreasing subsequently.

The empirical formulas in Eqs. (13)–(15) do not consider the thermal buoyancy.^{13,34,35} For the forced convection, the time-averaged Nusselt number is expressed by a power law relationship¹³ as $Nu_{\text{mean}} = CR^{m}Pr^n$. On this basis, the empirical formulas of Nu_{mean} of each cylinder in the mixed convection are summarized in Eq. (16). It is noted that when $Ri = 0$, the empirical formula is equal to that of forced convection. Meanwhile, the precision of each formula is checked. The maximum error of C1's formula is less than 4.36%, and it is less than 4.77% and 3.90% for C2 and C3, respectively,

$$Nu_{\text{mean}} = 0.618Re^{0.5}Pr^{0.333}1.02^{Ri} \quad (\text{C1}), \quad (16a)$$

$$Nu_{\text{mean}} = 0.501Re^{0.5}Pr^{0.333}1.10^{Ri} \quad (\text{C2}), \quad (16b)$$

$$Nu_{\text{mean}} = 0.326Re^{0.5}Pr^{0.333}1.25^{Ri} \quad (\text{C3}). \quad (16c)$$

Figure 11 shows the standard deviation of the Nusselt number Nu_{rms} with respect to Pr , which represents the global pulsation intensity for each cylinder. For C1, it shows that the Nu_{rms} increases slowly with the increase in Pr . At low Prandtl number, temperature gradients are less steep.³⁶ It is noted that Nu_{rms} increases when $Ri < 1$, while

FIG. 10. Variation of the mean Nusselt number over the time with respect to Pr : upstream cylinder C1 (left), middle cylinder C2 (middle), and downstream cylinder C3 (right).

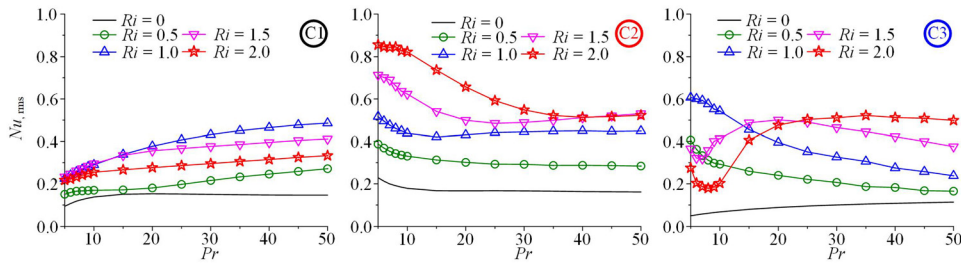


FIG. 11. Variation of the standard deviation Nusselt number Nu_{rms} with respect to Pr : upstream cylinder C1 (left), middle cylinder C2 (middle), and downstream cylinder C3 (right).

decreasing when $Ri \geq 1$ at the same Pr . The Nu_{rms} at $Ri = 0$ converges to about 0.147 at high Pr . For C2, the Nu_{rms} decreases with Pr , due to the weakened cross thermal buoyancy. The Nu_{rms} at $Ri = 0$ converges to about 0.162 at high Pr . For C3 at $Ri = 0$, the Nu_{rms} increases with

Pr and reaches a nearly constant value of 0.113. The Nu_{rms} decreases with Pr at $Ri = 0.5$ and 1.0. It is noted that the Nu_{rms} decreases at small Pr ($Pr \leq 7$ for $Ri = 1.5$ and $Pr \leq 8$ for $Ri = 2.0$), and then increases when $Pr \leq 20$, and decreases when $Pr > 20$ as Pr increases.

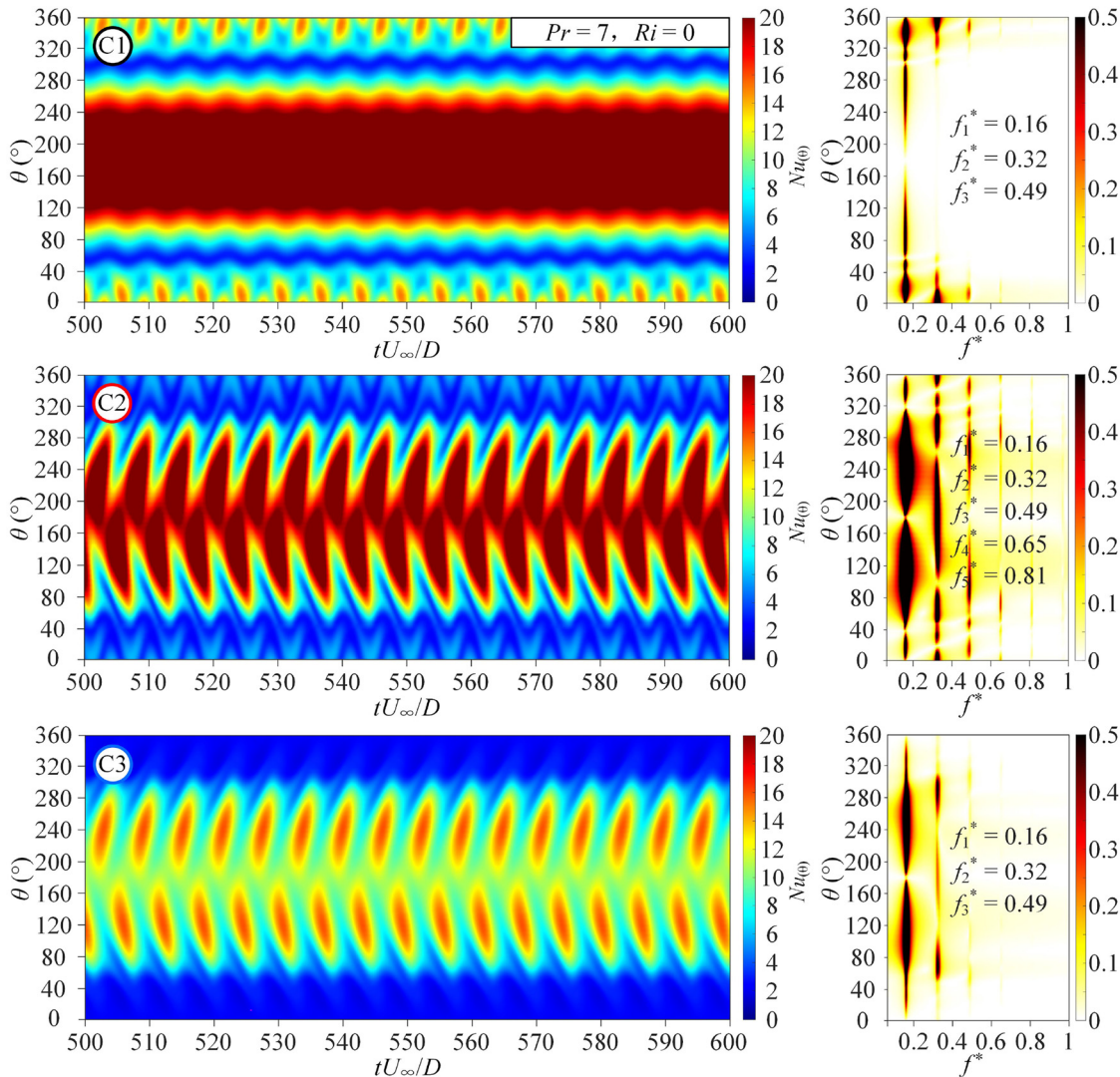


FIG. 12. The spatial-temporal evolution of $Nu_{(\theta)}$ (left) and frequency (right) around the cylinders' surface at $Pr = 7$ in forced convection ($Ri = 0$).

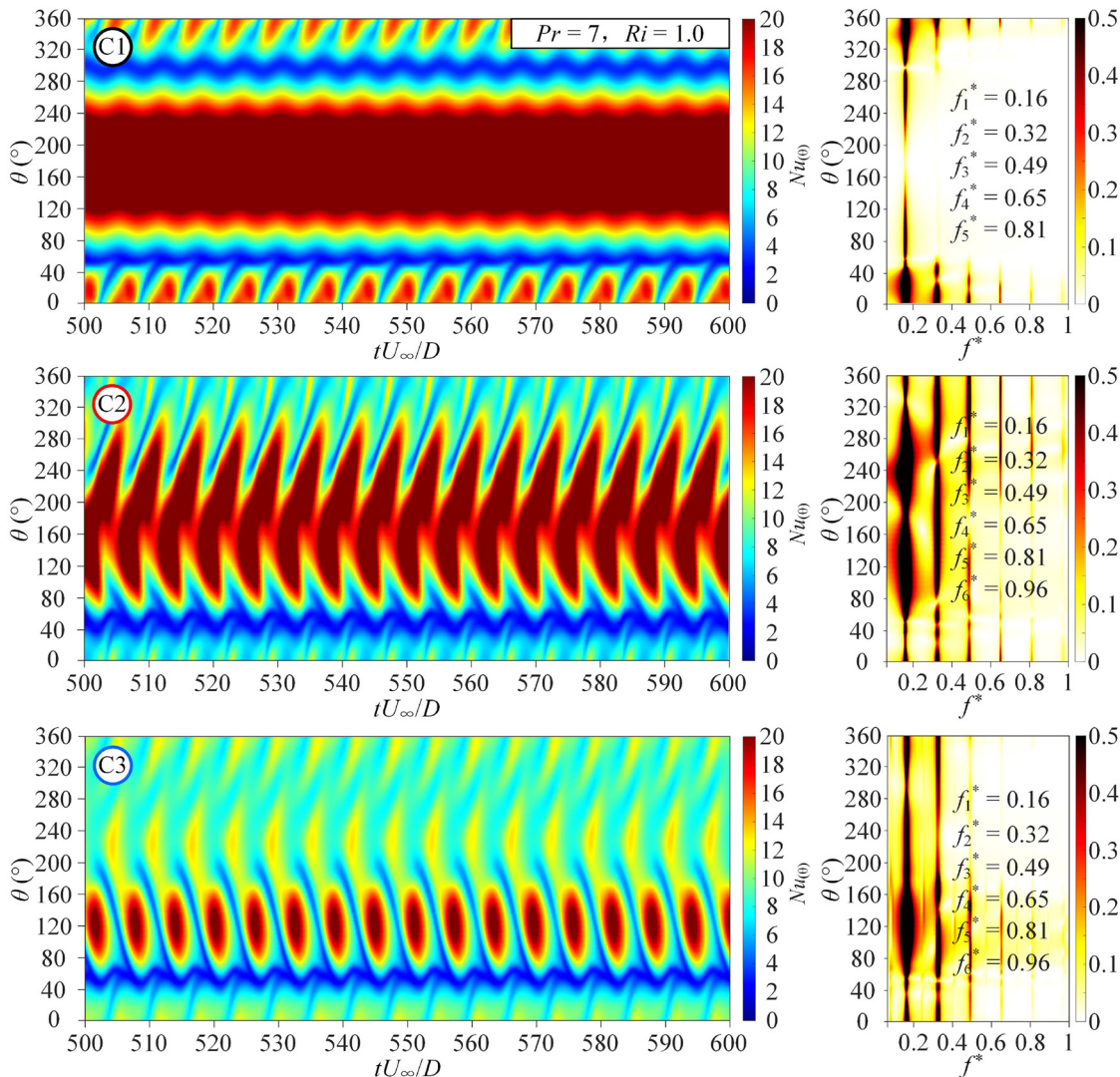


FIG. 13. The spatial-temporal evolution of $Nu(\theta)$ (left) and frequency (right) around the cylinders' surface at $Pr=7$ in mixed convection ($Ri=1.0$).

Water has a Prandtl number of about 7. Therefore, Figs. 12–14 show the time histories of the $Nu(\theta)$ and frequency distribution at $Pr=7$ along the tandem cylinders' surface measured counterclockwise from the rear stagnation point ($\theta=0^\circ$).¹⁵ It can be seen that the fluctuation of heat convection on both sides of the cylinders is symmetric in the forced convection ($Ri=0$), while asymmetric in the mixed convection ($Ri=1.0$ and 2.0). Moreover, this asymmetry is significantly enhanced with increasing the Ri , while being suppressed with increasing the Pr . The periodic and alternatively shed vortices cause the continuous exchange of fluid momentum and thermal energy in the wake, resulting in the fluctuation of the local $Nu(\theta)$ along the cylinder's surface.¹⁵ Meanwhile, the thermal boundary layer of C1 at the front stagnation point is quite thin, leading to a large local temperature gradient.

When $Ri=0$ (forced convection), as shown in Fig. 12, the $Nu(\theta)$ distribution along the cylinder's surface is symmetry about the

centerline. For C1, the variation of $Nu(\theta)$ mainly occurs around the rear stagnation point (0° or 360°). Consequently, the spatial distribution of the dimensionless frequency f^* ($=fD/u_{in}$) of $Nu(\theta)$ is mainly contributed from the rear stagnation point. The dominant frequency is $f_1^*=0.16$, the secondary frequency f_2^* is about two times of f_1^* , and the third frequency f_3^* is about three times of f_1^* . For C2, as stated in Sec. V B, the shedding vortices alternately reattach on the C2 surface, the violent variation of $Nu(\theta)$ occurs around the cylinder surface in the region of $40^\circ\text{--}180^\circ$ and $180^\circ\text{--}320^\circ$. Furthermore, the fifth frequency f_5^* is observed, which is about five times of f_1^* . For C3, the value of $Nu(\theta)$ decreases remarkably, due to the quasi-co-shedding²⁸ wake structure. The heat convection of C3 is suppressed by the double row vortices shed from C2. Moreover, the variation of $Nu(\theta)$ region is similar to that of C2, and the third frequency $f_3^*=0.49$ is observed, which is approximately three times of f_1^* .

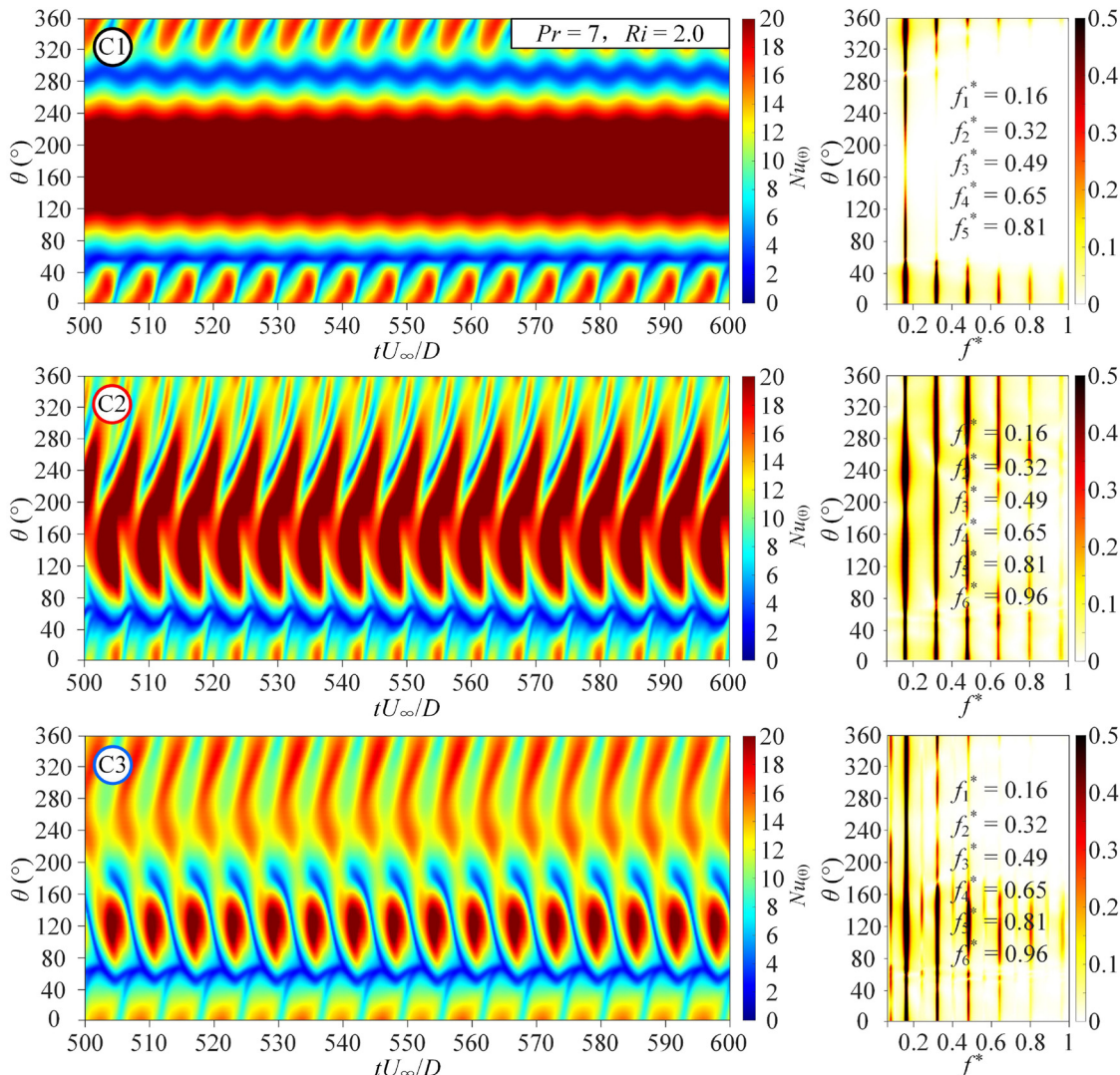


FIG. 14. The spatial-temporal evolution of $Nu_{(\theta)}$ (left) and frequency (right) around the cylinders' surface at $Pr = 7$ in mixed convection ($Ri = 2.0$).

When $Ri = 1.0$ (mixed convection), as shown in Fig. 13, the $Nu_{(\theta)}$ distribution along the cylinder's surface is asymmetry about the centerline. For C1, the dominant frequency of $Nu_{(\theta)}$ around the rear surface is about $f_1^* = 0.16$. Meanwhile, the secondary and third frequencies are also observed around the rear stagnation point. This phenomenon is confirmed in the cases of the forced ($Ri = 0$) and mixed convection ($Ri > 0$), where the strong mixing occurs.¹⁵ For C2, more plentiful harmonic frequencies are observed due to the cross thermal buoyancy, and the frequency contours of $Nu_{(\theta)}$ become asymmetric about the centerline. For C3, the $Nu_{(\theta)}$ increases distinctly, being larger than the case of forced convection ($Ri = 0$). The violent variation of $Nu_{(\theta)}$ occurs around the lower surface in the region of 80° – 160° , as shown in Fig. 13. Moreover, the sixth frequency $f_6^* = 0.96$ is observed, which is approximately six times of f_1^* .

When Ri increases to 2, as shown in Fig. 14, the asymmetry becomes stronger and the $Nu_{(\theta)}$ increases. The spatial-temporal evolution of $Nu_{(\theta)}$ and frequency around the C1 surface change slightly. Therefore, the Nu_{mean} of C1 is independent of Ri at the same Pr . The pattern of spatial-temporal evolution of $Nu_{(\theta)}$ for C2 is similar to $Ri = 1.0$, but the heat exchange is enhanced. For C3, the $Nu_{(\theta)}$ is strengthened in both lower and upper sides. Consequently, the sixth frequency $f_6^* = 0.96$ is observed more intuitively.

D. Characteristics of fluid kinetic energy and thermal energy in the wake

The transportation of fluid kinetic energy and thermal energy in forced and mixed convection is discussed. The normalized time-averaged velocities u_{mean} and v_{mean} and the time-averaged pressure coefficient C_p_{mean} and temperature T_{mean} are defined as

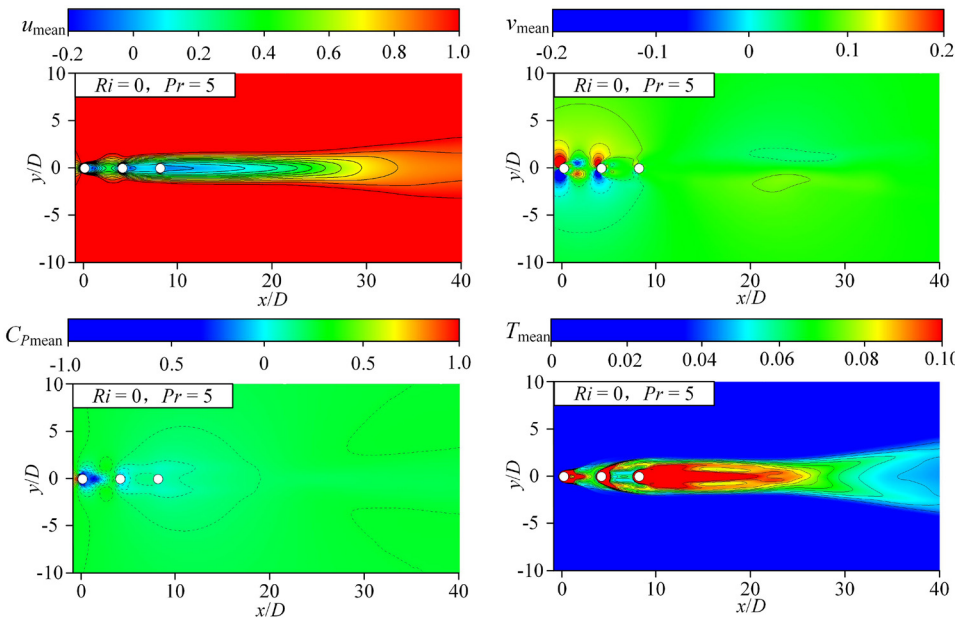


FIG. 15. The normalized time-averaged velocities u_{mean} and v_{mean} and the time-averaged pressure coefficient $C_{P\text{mean}}$ and temperature T_{mean} at $Ri = 0$ and $Pr = 5$.

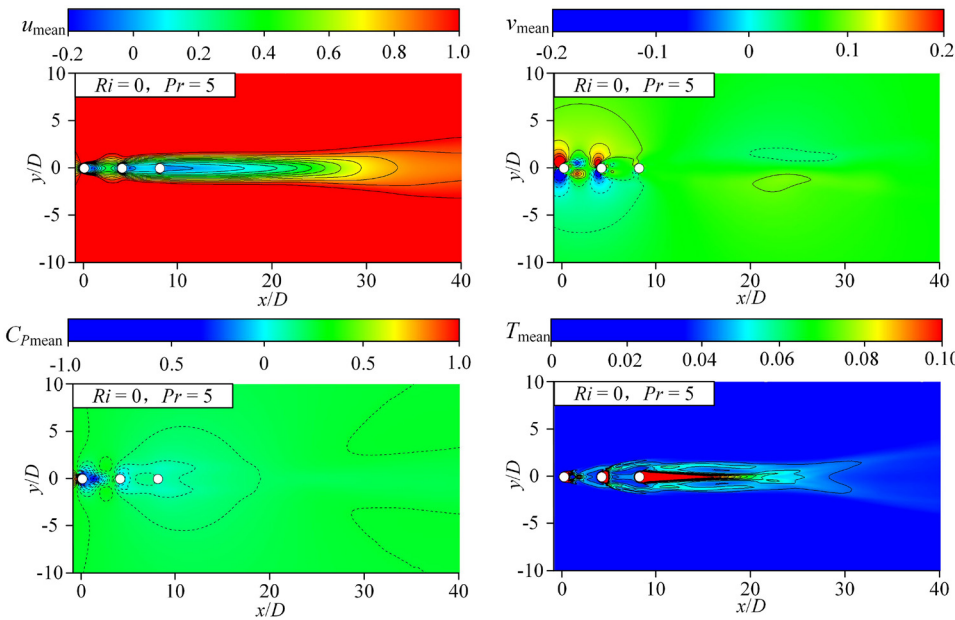


FIG. 16. The normalized time-averaged velocities u_{mean} and v_{mean} and the time-averaged pressure coefficient $C_{P\text{mean}}$ and temperature T_{mean} at $Ri = 0$ and $Pr = 50$.

$$u_{\text{mean}} = \frac{1}{N} \sum_{t=1}^N u_t, \quad (17a)$$

$$v_{\text{mean}} = \frac{1}{N} \sum_{t=1}^N v_t, \quad (17b)$$

$$C_{P\text{mean}} = \frac{1}{N} \sum_{t=1}^N C_{Pt}, \quad (17c)$$

$$T_{\text{mean}} = \frac{1}{N} \sum_{t=1}^N T_t, \quad (17d)$$

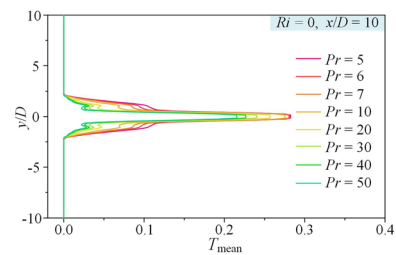


FIG. 17. The transverse temperature distribution in the wake at $x/D = 10$.

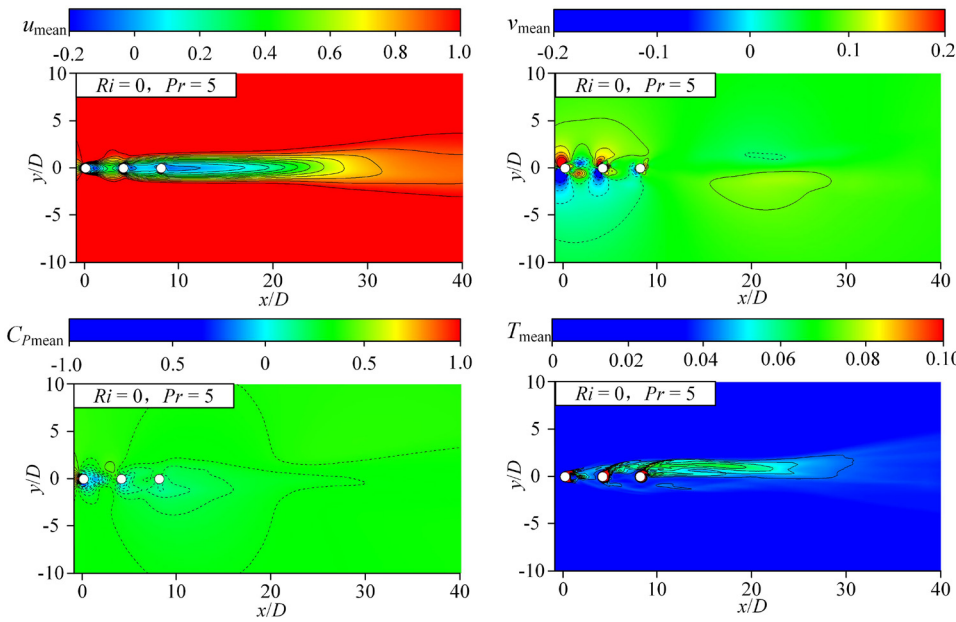


FIG. 18. The normalized time-averaged velocities u_{mean} and v_{mean} and the time-averaged pressure coefficient $C_{P\text{mean}}$ and temperature T_{mean} at $Ri = 1.0$ and $Pr = 7$.

where N is the number of sampled data in the time series, u_b , v_b , C_{Pb} , and T_b are the instant streamwise velocity, transverse velocity, pressure coefficient, and temperature, respectively. In forced convection ($Ri = 0$), the coherent structures of the vortex dynamics and thermal diffusion are symmetric.¹⁵ Figure 15 shows the contours of u_{mean} , v_{mean} , $C_{P\text{mean}}$, and T_{mean} at $Ri = 0$ and $Pr = 5$, respectively. The characteristics of fluid kinetic energy and thermal energy in the wake of three

heated circular cylinders in forced convection are all symmetric about the centerline. The width of u_{mean} contours increases after $x/D \approx 30$, due to the secondary vortex street formation. The contour of v_{mean} is in consistent with reported result²⁸ for three tandem cylinders without heat convection at $Re = 160$. It shows that the transverse velocity around the C3 surface is very small. The differences of $C_{P\text{mean}}$ between the front and rear surfaces of C1 is larger than that of C2 and C3,

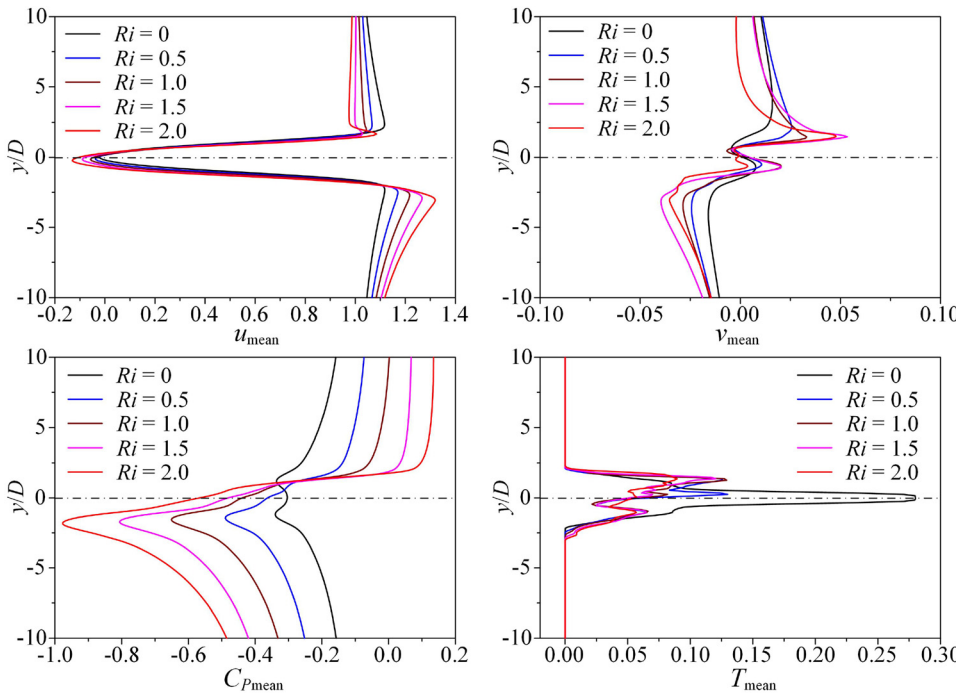


FIG. 19. The transverse distribution of u_{mean} , v_{mean} , $C_{P\text{mean}}$, and T_{mean} at $Pr = 7$ in the wake at $x/D = 10$.

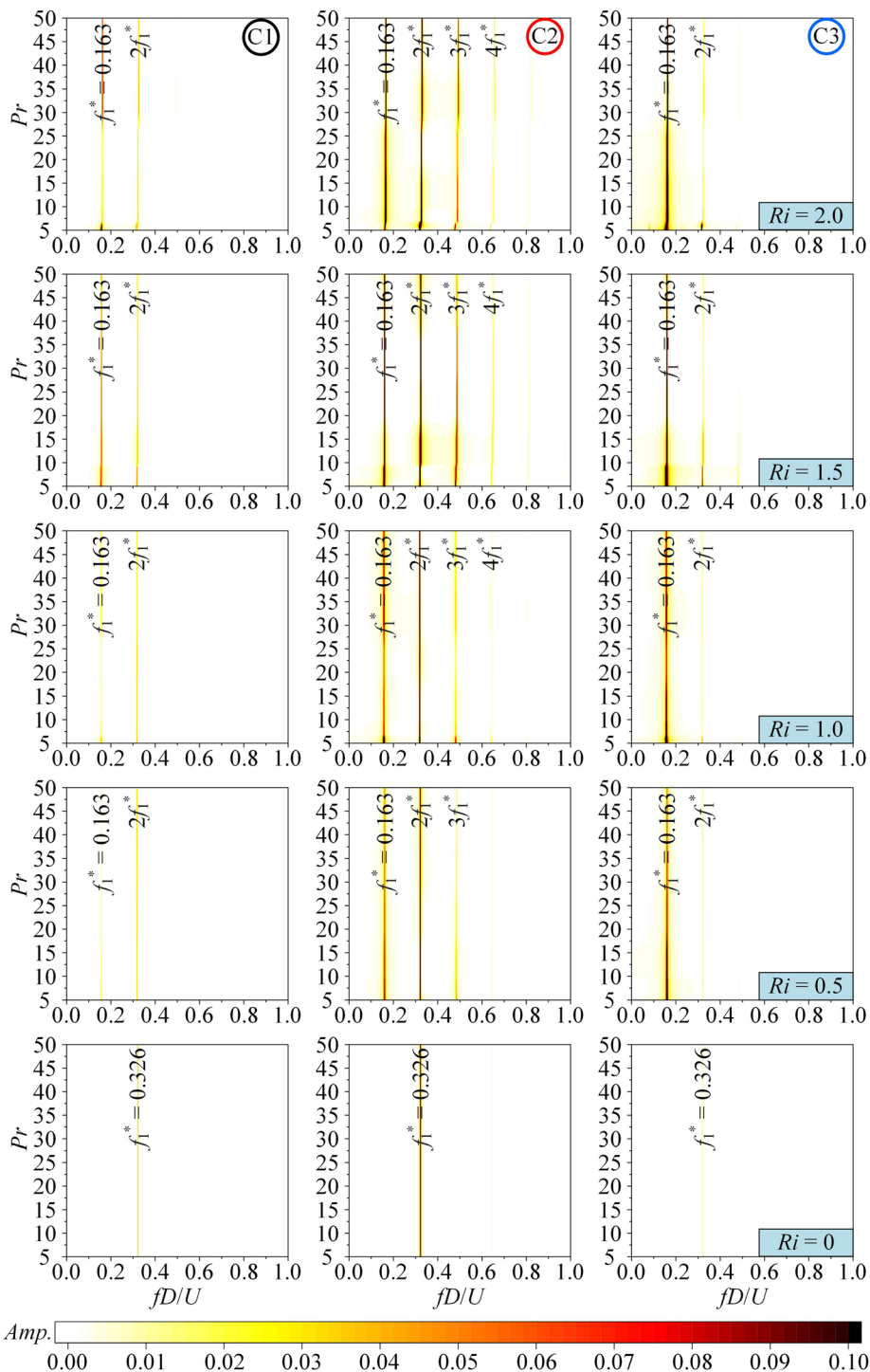


FIG. 20. Variation of the frequency of drag coefficient for different Ri and Pr .

which confirms that the time-averaged drag coefficient $C_{D,\text{mean}}$ of C1 is larger than that of C2 and C3. The spatial gradient distribution of temperature is mainly concentrated behind C3 and rapidly decline around the secondary vortex formation position at $x/D \approx 30$.

When Pr increases to 50, as depicted in Fig. 16, the momentum transfer is unaffected by the heat transfer, due to the irrespective of energy and temperature in the continuity equation and momentum equation. Therefore, the normalized time-averaged

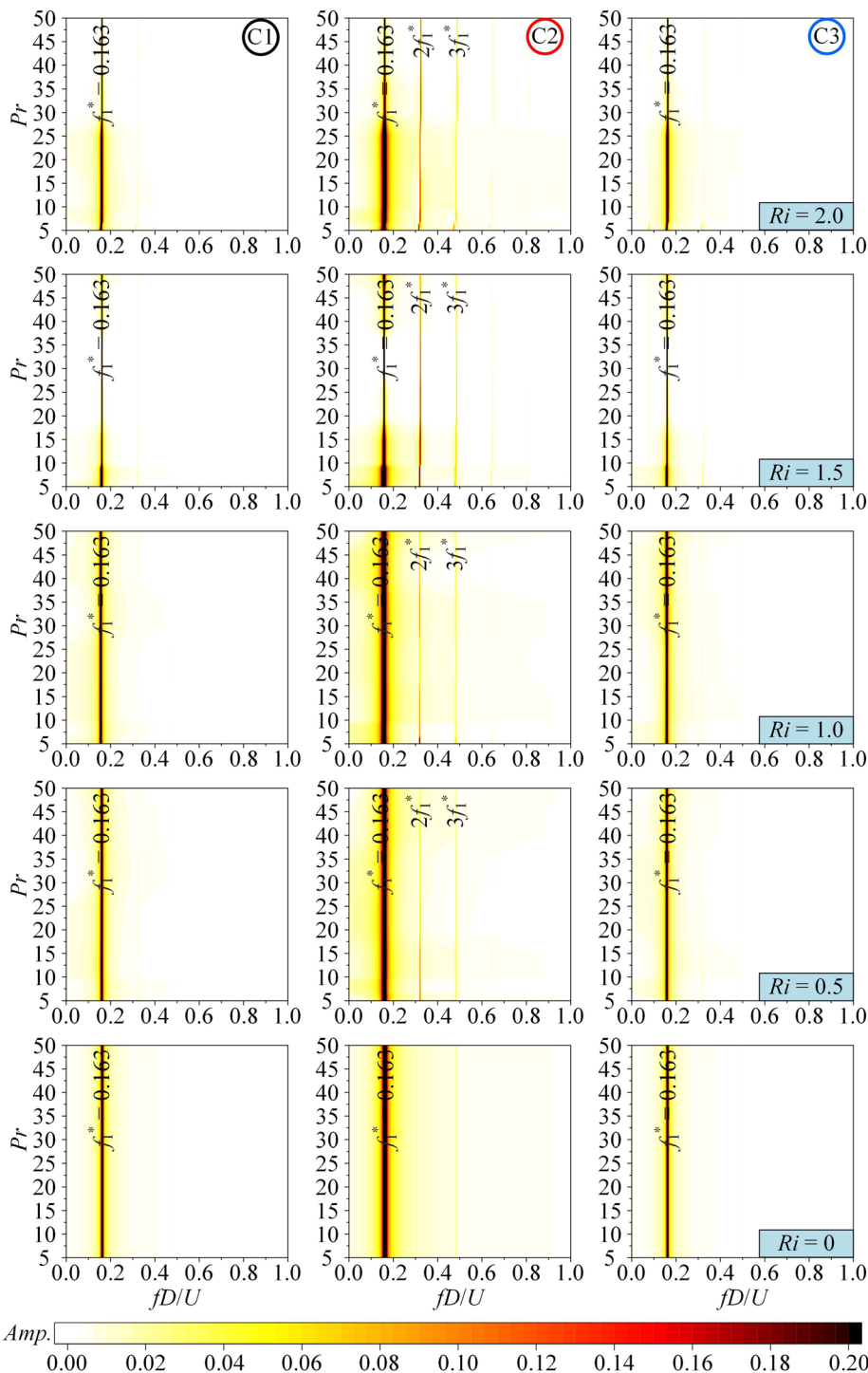


FIG. 21. Variation of the frequency of lift coefficient for different Ri and Pr .

velocities u_{mean} and v_{mean} and the time-averaged pressure coefficient $C_{P\text{mean}}$ are the same as the case of $Pr=5$. However, the increase in Pr sets higher temperature gradients over the cylinder surfaces, and thereby a higher rate of heat transfer, a thinner

thermal boundary layer and a smaller region of the spatial gradient distribution of temperature.

To further investigate the heat transfer behavior in the wake, the transverse time-averaged temperature distribution³⁷ at $x/D=10$ is

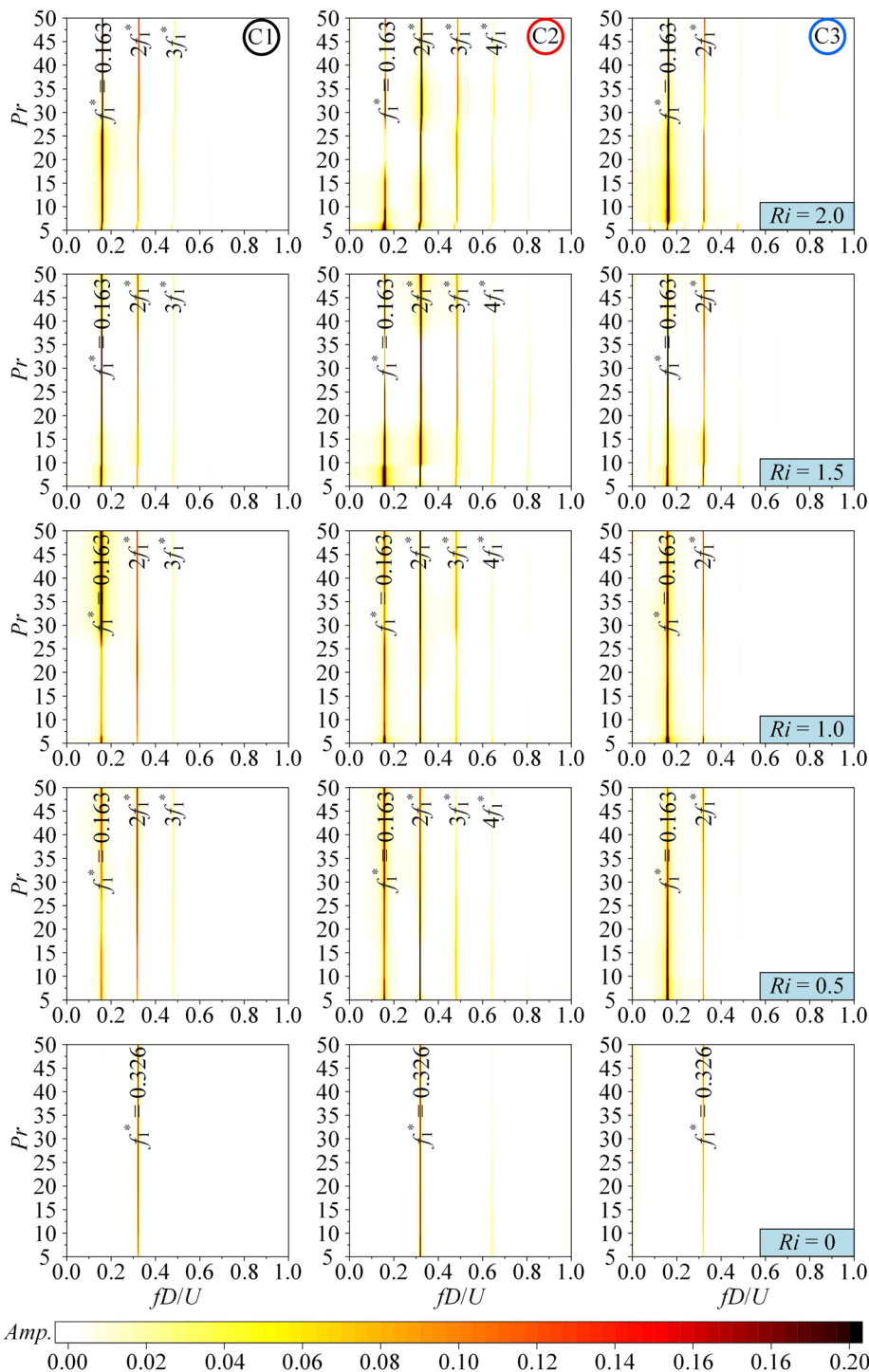


FIG. 22. Variation of the frequency of Nusselt number over the cylinder for different Ri and Pr .

extracted in Fig. 17. The high temperature region is mainly located around $y/D = 0$, which is in consistent with the temperature contours. The extreme maximum value of T_{mean} at the centerline decreases with Pr . It is noted that there is only one peak value of T_{mean} when $Pr < 10$,

while three peak values are observed when $Pr \geq 10$ and the two other peaks are symmetric about the centerline. This is because the thermal shear layer of C2 does not merge with that of C3, as shown in Figs. 15 and 16.

When $Ri > 0$ (mixed convection), the cross thermal buoyancy obviously affects the wake structure. The impairment of the baroclinic vorticity production is provoked by the spanwise temperature gradient.³⁶ Consequently, the characteristics of fluid kinetic energy and thermal energy in wake are asymmetric about the centerline. Figure 18 shows the contours of u_{mean} , v_{mean} , $C_{P\text{mean}}$, and T_{mean} at $Ri = 1.0$ and $Pr = 7$, respectively.

Figure 19 shows the transverse distribution of u_{mean} , v_{mean} , $C_{P\text{mean}}$, and T_{mean} at $Pr = 7$ in the wake at $x/D = 10$. The value of u_{mean} in the upper side decreases with Ri , while increasing in the lower side. It implies that the streamwise velocity in the upper side is suppressed, while it is accelerated in the lower side due to the cross thermal buoyancy. The transverse time-averaged velocity gets more asymmetry. The time-averaged pressure coefficient $C_{P\text{mean}}$ in the upper side increases while decreasing in the lower side with increasing the Ri . Moreover, the thermal buoyancy observably weakens the heat transfer, resulting in the decrease in T_{mean} , as shown in Fig. 19.

E. Frequency

To figure out the frequency relation of three heated tandem circular cylinders in forced convection ($Ri = 0$) and mixed convection ($Ri > 0$), the amplitude spectral density (ASD)¹⁵ contours of the hydrodynamic coefficients (C_D and C_L) and Nusselt number (Nu) are plotted in Figs. 20–22. As shown in Fig. 20, the ASD contours of C_D remain constant with the increase in Pr for the cases of forced convection ($Ri = 0$). The value of the dominant frequency of each cylinder is 0.326. However, when $Ri > 0$, in the cases of mixed convection, the dominant frequency of C_1 changes to 0.163, which is a half of 0.326. The ASD of the dominant frequency increases with Ri , then shifts to 0.163 when $Ri > 1.0$. For C_2 , under the influence of cross thermal buoyancy, more harmonic frequencies appear at $Ri > 0$, and the dominant frequency is hard to find out. For C_3 , the dominant frequency changes to 0.163 in the mixed convection ($Ri > 0$), and the associated ASD increases with Ri .

Figure 21 shows the ASD contours of C_L for different Ri and Pr . It is noted that the value of the dominant frequency of each cylinder is 0.163, which is a half of 0.326. Moreover, the second and third frequencies are observed on C_2 when $Ri > 0$, which are two and three times the dominant one. In addition, the frequency spectrum of heat convection (Nu) is similar to that of C_D , as shown in Fig. 22. It means that the frequency of Nu is dominated by the drag force, which has been reported in the literature.²⁴

VI. CONCLUSIONS

In this study, the wake and heat transfer characteristics of three tandem circular cylinders with a fixed spacing ratio of 4.0 in both forced and mixed convection flows were numerically investigated using the finite element method. The computations were carried out in the range of Prandtl number $Pr = 5\text{--}50$ and Richardson number $Ri = 0\text{--}2$ at a low Reynolds number of $Re = 150$. The thermal buoyancy has a significant effect on the wake pattern in the mixed convection. The symmetric feature of the entire flow field breaks down due to the presence of cross buoyancy when $Ri > 0$.

An adequate parameter to describe the vorticity accumulation and structure formation is the squared strain rate minus the square of the vorticity $\gamma = \frac{1}{2}(\sigma_1^2 + \sigma_2^2 - \omega^2)$, which provides a quantity to describe the vortex-shedding and enstrophy transfer process. Thermal

plume structures at further downstream originate from the upper dispersed vortex due to the high superimposed buoyancy at low Pr , while being suppressed at high Pr . The shedding of the lower vortex is more concentrated, while the upper vortex is dispersed. The upward buoyancy force seems to prevent the formation of the coherent vortex structures. The increase in Pr plays a role as the flow stabilization, while Ri plays the reverse role.

The time-averaged drag coefficient $C_{D,\text{mean}}$, the standard deviation drag coefficient $C_{D,\text{rms}}$, the time-averaged lift coefficient $C_{L,\text{mean}}$, and the standard deviation lift coefficient $C_{L,\text{rms}}$ vary with the Pr and converge to a nearly constant value at larger Pr , depending on the Ri . The symmetry wake about the centerline is destroyed and each cylinder encounters a negative $C_{L,\text{mean}}$ with the presence of cross thermal buoyancy when $Ri > 0$. The correlation of the mean Nusselt number Nu_{mean} in the forced convection conforms to a power law relationship as $Nu_{\text{mean}} = CR^{m}Pr^n$. Three empirical formulas of Nu_{mean} in the mixed convection are proposed as $Nu_{\text{mean}} = C_1Re^mPr^nC_2^{Ri}$. When $Ri = 0$, the empirical formula follows the forced convection form. The migration of the shear layer due to the thermal buoyancy results in the frequency migration and harmonic frequencies in the drag, lift and Nusselt coefficients.

ACKNOWLEDGMENTS

The research work was supported by the National Natural Science Foundation of China (Nos. 51979238 and 52301338) and the Sichuan Science and Technology Program (Nos. 2023NSFSC1953 and 2023ZYD0140). The work was carried out in the computer cluster of the laboratory of offshore oil and gas engineering at Southwest Petroleum University. The authors appreciate the support from the Offshore Oil and Gas Laboratory at Southwest Petroleum University.

AUTHOR DECLARATIONS

Conflict of Interest

The authors have no conflicts to disclose.

Author Contributions

Hongjun Zhu: Conceptualization (equal); Funding acquisition (equal); Methodology (equal); Resources (equal); Supervision (equal); Writing – review & editing (equal). **Jiawen Zhong:** Formal analysis (equal); Investigation (equal); Visualization (equal); Writing – original draft (equal). **Bin Liu:** Methodology (equal); Software (equal); Validation (equal). **Tongming Zhou:** Supervision (equal); Writing – review & editing (equal).

DATA AVAILABILITY

The data that support the findings of this study are available from the corresponding author upon reasonable request.

NOMENCLATURE

C_D	drag coefficient ($=2F_D/\rho U_\infty^2 D$)
C_L	lift coefficient ($=2F_L/\rho U_\infty^2 D$)
D	projected length square cylinder (m)

F_D	drag force per unit length of cylinder (N/m)
F_L	lift force per unit length of cylinder (N/m)
f	frequency of vortex shedding (1/s)
Gr	Grashof number ($=g\beta(T_w-T_\infty)D^3/v^2$)
g	acceleration due to gravity (m/s ²)
Nu	mean Nusselt number over the cylinder surface
Nu_{mean}	mean Nusselt number over the time of cylinder
$Nu_{(s)}$	local Nusselt number
Pr	Prandtl number (ν/κ)
Re	Reynolds number ($=\rho u_{\text{in}} D / \mu$)
Ri	Richardson number ($=Gr/Re^2$)
St	Strouhal number ($=fD/u_{\text{in}}$)
T_∞	temperature of the free stream (K)
T_w	temperature of the cylinder (K)
t	time (s)
u_{in}	free stream velocity (m/s)
x, y	dimensionless coordinates

Greek symbols

α	angle of the inlet velocity with buoyancy
β	coefficient of thermal expansion (1/K)
κ	thermal diffusivity of fluid (m ² /s)
μ	dynamic viscosity of fluid (Pa s)
ν	kinematic viscosity of fluid (m ² /s)
ρ	density of fluid (kg/m ³)

Subscripts

mean	time-averaged
∞	inlet condition

REFERENCES

- ¹N. V. V. K. Chaitanya, S. Khambra, and D. Chatterjee, "Mixed convective transport around tandem circular cylinders in an unconfined medium," *Nucl. Eng. Des.* **419**, 112969 (2024).
- ²H. Zhu, Y. Li, J. Zhong, and T. Zhou, "Numerical investigation on the effect of bionic fish swimming on the vortex-induced vibration of a tandemly arranged circular cylinder," *Phys. Fluids* **36**, 037146 (2024).
- ³F. Zafar and M. M. Alam, "Mixed convection heat transfer from a circular cylinder submerged in wake," *Int. J. Mech. Sci.* **183**, 105733 (2020).
- ⁴H. Hu and M. M. Koochesfahani, "The wake behavior behind a heated cylinder in forced and mixed convection regimes," in *ASME 2005 Summer Heat Transfer Conference* (ASME, 2005), pp. 745–756.
- ⁵H. Badr, "A theoretical study of laminar mixed convection from a horizontal cylinder in a cross stream," *Int. J. Heat Mass Transfer* **26**, 639–653 (1983).
- ⁶R. N. Kieft, C. C. M. Rindt, and A. A. van Steenhoven, "The wake behaviour behind a heated horizontal cylinder," *Exp. Therm. Fluid Sci.* **19**, 183–193 (1999).
- ⁷R. N. Kieft, C. C. M. Rindt, A. A. van Steenhoven, and G. J. F. van Heijst, "On the wake structure behind a heated horizontal cylinder in cross-flow," *J. Fluid Mech.* **486**, 189–211 (2003).
- ⁸W. J. P. M. Maas, C. C. M. Rindt, and A. A. van Steenhoven, "The influence of heat on the 3D-transition of the von Kármán vortex street," *Int. J. Heat Mass Transfer* **46**, 3069–3081 (2003).
- ⁹R. Grundmann and O. Posdziech, "Numerical simulation of the flow around an infinitely long circular cylinder in the transition regime," *Theor. Comput. Fluid Dyn.* **15**, 121–141 (2001).
- ¹⁰H. Jiang, L. Cheng, S. Draper, H. An, and F. Tong, "Three-dimensional direct numerical simulation of wake transitions of a circular cylinder," *J. Fluid Mech.* **801**, 353–391 (2016).
- ¹¹C. H. K. Williamson, "Vortex dynamics in the cylinder wake," *Annu. Rev. Fluid Mech.* **28**, 477–539 (1996).
- ¹²G. Biswas and S. Sarkar, "Effect of thermal buoyancy on vortex shedding past a circular cylinder in cross-flow at low Reynolds numbers," *Int. J. Heat Mass Transfer* **52**, 1897–1912 (2009).
- ¹³S. Sarkar, A. Dalal, and G. Biswas, "Unsteady wake dynamics and heat transfer in forced and mixed convection past a circular cylinder in cross flow for high Prandtl numbers," *Int. J. Heat Mass Transfer* **54**, 3536–3551 (2011).
- ¹⁴S. A. Kumar, M. Mathur, A. Sameen, and S. Anil Lal, "Effects of Prandtl number on the laminar cross flow past a heated cylinder," *Phys. Fluids* **28**, 113603 (2016).
- ¹⁵H. Zhu, J. Zhong, and B. Liu, "Hydro- and thermo-dynamic characteristics of a circular cylinder placed in mixed convection flow," *Phys. Fluids* **34**, 093614 (2022).
- ¹⁶H. Garg, A. K. Soti, and R. Bhardwaj, "Vortex-induced vibration and galloping of a circular cylinder in presence of cross-flow thermal buoyancy," *Phys. Fluids* **31**, 113603 (2019).
- ¹⁷B. Liu and H. Zhu, "Secondary lock-in of vortex-induced vibration and energy transfer characteristics of a vibrating cylinder subject to cross buoyancy," *Phys. Fluids* **33**, 073607 (2021).
- ¹⁸L. Houssem and B. Mohamed, "Mixed convection heat transfer from confined tandem circular cylinders in cross-flow at low Reynolds number," *Mechanika* **23**, 522–527 (2017).
- ¹⁹L. Houssem, B. Blissag, and B. Mohamed, "The flow and mixed convection around tandem circular cylinders at low Reynolds number," *Defect Diffus. Forum* **378**, 59–67 (2017).
- ²⁰A. N. Brooks and T. J. R. Hughes, "Streamline upwind/Petrov–Galerkin formulations for convection dominated flows with particular emphasis on the incompressible Navier–Stokes equations," *Comput. Methods Appl. Mech. Eng.* **32**, 199–259 (1982).
- ²¹T. J. Hughes, L. P. Franca, and M. Balestra, "A new finite element formulation for computational fluid dynamics: V. Circumventing the Babuška–Brezzi condition: A stable Petrov–Galerkin formulation of the Stokes problem accommodating equal-order interpolations," *Comput. Methods Appl. Mech. Eng.* **59**, 85–99 (1986).
- ²²J. Chung and G. M. Hulbert, "A time integration algorithm for structural dynamics with improved numerical dissipation: The generalized- α method," *J. Appl. Mech.* **60**, 371–375 (1993).
- ²³K. E. Jansen, C. H. Whiting, and G. M. Hulbert, "A generalized- α method for integrating the filtered Navier–Stokes equations with a stabilized finite element method," *Comput. Methods Appl. Mech. Eng.* **190**, 305–319 (2000).
- ²⁴T. K. Prasanth, S. Behara, S. P. Singh, R. Kumar, and S. Mittal, "Effect of blockage on vortex-induced vibrations at low Reynolds numbers," *J. Fluids Struct.* **22**, 865–876 (2006).
- ²⁵M. Zhao, F. Tong, and L. Cheng, "Numerical simulation of two-degree-of-freedom vortex-induced vibration of a circular cylinder between two lateral plane walls in steady currents," *J. Fluids Eng.* **134**, 104501 (2012).
- ²⁶H. Zhu, J. Zhong, and B. Liu, "Fluid–thermal–structure interaction of three heated circular cylinders in tandem at a low Reynolds number of 150," *Phys. Fluids* **34**, 083605 (2022).
- ²⁷V. D. Duong, V. D. Nguyen, V. T. Nguyen, and I. L. Ngo, "Low-Reynolds-number wake of three tandem elliptic cylinders," *Phys. Fluids* **34**, 043605 (2022).
- ²⁸H. Zhu, J. Zhong, and T. Zhou, "Wake structure characteristics of three tandem circular cylinders at a low Reynolds number of 160," *Phys. Fluids* **33**, 044113 (2021).
- ²⁹R. Kieft, C. C. M. Rindt, and A. A. van Steenhoven, "Near-wake effects of a heat input on the vortex-shedding mechanism," *Int. J. Heat Fluid Flow* **28**, 938–947 (2007).
- ³⁰J. Weiss, "The dynamics of enstrophy transfer in two-dimensional hydrodynamics," *Physica D* **48**, 273–294 (1991).
- ³¹M. M. Alam, M. Moriya, K. Takai, and H. Sakamoto, "Fluctuating fluid forces acting on two circular cylinders in a tandem arrangement at a subcritical Reynolds number," *J. Wind Eng. Ind. Aerodyn.* **91**, 139–154 (2003).
- ³²H. Zhu, J. Zhong, and J. Song, "Study on the wake interference and dynamic evolution characteristics of the fluid–structure interaction of three

tandem circular cylinders," *Chin. J. Theor. Appl. Mech.* **56**, 1178–1186 (2024).

³³A. R. Dwivedi and A. K. Dhiman, "Flow and heat transfer analysis around tandem cylinders: Critical gap ratio and thermal cross-buoyancy," *J. Braz. Soc. Mech. Sci. Eng.* **41**, 487 (2019).

³⁴S. W. Churchill and M. Bernstein, "A correlating equation for forced convection from gases and liquids to a circular cylinder in crossflow," *J. Heat Transfer* **99**, 300–306 (1977).

³⁵W. A. Khan, J. R. Culham, and M. M. Yovanovich, "Fluid flow around and heat transfer from an infinite circular cylinder," *J. Heat Transfer* **127**, 785–790 (2005).

³⁶S. Rolfo, K. Kopsidas, S. A. Rahman, C. Moulinec, and D. R. Emerson, "Effect of large scale 3-D structures on the flow around a heated cylinder at low Reynolds number," *Flow Turbul. Combust.* **101**, 553–577 (2018).

³⁷S. Yu, T. Tang, J. Li, and P. Yu, "Wake and thermal characteristics for cross-buoyancy mixed convection around and through a porous cylinder," *Phys. Fluids* **32**, 073603 (2020).